The Emissivity of the Ocean Surface Between 6 and 90 GHz Over a Large Range of Wind Speeds and Earth Incidence Angles

Thomas Meissner, *Member, IEEE*, and Frank J. Wentz

***Abstract*—We present a model function for the emissivity of the wind roughened ocean surface for microwave frequencies between 6 and 90 GHz. It is an update, refinement, and extension of model functions we had developed previously. The basis of our analysis are brightness temperature (TB) measurements from the spaceborne microwave radiometer WindSat and the Special Sensor Microwave/Imager, which are collocated with independent measurements of surface wind speeds and directions. This allows the determination of the emissivity model function for Earth incidence angles (EIA) around 55°. We demonstrate that an essential part in the model development is the absolute calibration of the radiometer measurements over the ocean to the computed TB of the radiative transfer model, one of whose components the emissivity model function is. We combine our results with other established measurements for lower EIA and finally obtain a model function which can be used over the whole EIA range between 0° and 65°. Results for both the isotropic, wind direction independent part as well as the four Stokes parameters of the wind direction signal are presented. Special emphasis is made on the behavior at high wind speeds between 20 and 40 m/s by conducting a comparison with data from the step frequency microwave radiometer.**

***Index Terms*—High wind speeds, microwave radiometer calibration, ocean surface emissivity, radiative transfer model (RTM), Step Frequency Microwave Radiometer (SFMR), Special Sensor Microwave/Imager (SSM/I), Stokes' parameters, WindSat.**

I. Introduction

ACCURATE knowledge of the microwave emissivity of the wind roughened ocean surface is crucial for the measurement of ocean environmental parameters from both spaceborne and airborne microwave radiometers. First of all, the wind-induced surface emissivity signal, which is sometimes also named excess emissivity, is the driver for measuring ocean surface wind speeds. In order to measure wind speeds to an accuracy of 1.0 m/s an accuracy in the surface emissivity signal of at least 1.0 K is required. Moreover, the wind-induced emissivity signal constitutes an unwanted source of noise for the retrievals of sea surface temperature (SST), sea surface salinity (SSS), columnar atmospheric water vapor, and liquid cloud water. The SST retrievals pose a particularly stringent requirement on the knowledge of the surface emissivity signal at C-band and X-band: an error of only 0.25 K in the C-band v-pol emissivity translates into an error of 0.50 K in the retrieved SST [1].

In general, the ocean surface emissivity is influenced by three different types of roughness scales.

1) Large gravity waves, whose wavelengths are long compared with the radiation wavelength. These large-scale waves mix vertical and horizontal polarizations and change the local incidence angle of the electromagnetic radiation.
2) Small gravity-capillary waves, which are riding on top of the large-scale waves, and whose RMS height is small compared with the radiation wavelength. These small-scale waves cause diffraction (Bragg scattering) of radiation that is backscattered from the ocean surface. From Kirchhoff's law, it follows that they also affect the passive microwave emission of the sea surface.
3) Sea foam, which arises as a mixture of air and water at the wind roughened ocean surface, and which leads to a general increase in the surface emissivity. This effect starts to become important at wind speeds above 7 m/s and becomes dominant at high wind speeds.

The emissivity signal that is produced by these mechanisms is largely isotropic, which means independent on wind direction, though there do exist anisotropic features which give rise to a small contribution that depends on the wind direction relative to the looking direction.

Numerous theoretical attempts have been made to model the wind-roughened ocean surface emissivity within two-scale ocean surface models [2]–[6], which incorporate the first two roughness scales mentioned above. The ocean surface is approximated by a two-scale surface where small-scale gravity-capillary waves ride on top of large-scale gravity waves. If the curvature of the large-scale waves is not too large, the geometric optics (GO) scattering model or Kirchhoff approximation can be used. Herein, the large-scale waves are modeled as an ensemble of tilted facets each acting individually as an infinitely large specular reflecting surface. The RMS height of the small-scale gravity-capillary waves is treated as a perturbative parameter and the electric field of the EM wave at the ocean surface is expanded up to second order in this perturbation. Though most of these models can give a good qualitative description of the wind-induced emissivity signal and its dependence on various parameters such as frequency, polarization, Earth incidence angles (EIA), wind speed, wind direction, or SST, unfortunately

Manuscript received April 8, 2011; revised September 4, 2011 and November 23, 2011; accepted November 29, 2011. Date of publication February 3, 2012; date of current version July 18, 2012.

The authors are with Remote Sensing Systems, Santa Rosa, CA 94501 USA (e-mail: meissner@remss.com; frank.wentz@remss.com).

Color versions of one or more of the figures in this paper are available online at http://ieeexplore.ieee.org.

Digital Object Identifier 10.1109/TGRS.2011.2179662

none of them provides the needed level of accuracy mentioned above.

It is therefore necessary to base the development of the wind-induced ocean emissivity on actual TB observations from airborne or spaceborne microwave radiometers that have been collocated to a measurement of the important surface parameters (wind speed, wind direction, SST). Essential is that these measurements are either themselves *in situ* ground truth observations or that they have been validated against ground truth measurements, and it has been checked that they are free of biases when compared to ground truth measurements. Those can be for example observations by buoys, ships, aircrafts, validated observations from scatterometers (QuikSCAT, ASCAT), or numerical weather prediction (NWP) models such as the National Centers for Environmental Prediction's General Data Assimilation System (NCEP GDAS). In tropical cyclones, we will also use the analysis of the National Oceanic Atmospheric Administration's (NOAA) Hurricane Research Division of Atlantic Oceanographic and Meteorological Laboratory (HRD) [7] (http://www.aoml.noaa.gov/hrd/index.html) as ground truth data for the development of our emissivity model.

The first major step in the development of a wind-induced emissivity model was done in [8]–[10], which used TB observations from both Special Sensor Microwave/Imager (SSM/I) and the Tropical Rainfall Measurement Mission Microwave Imager (TMI) sensor that were collocated with buoy wind speeds. An isotropic model function at W-band was developed in [11] using SSM/I TB over QuikSCAT wind speeds. With the availability of more microwave radiometer with a wider frequency range such as the Advanced Microwave Scanning Radiometer (AMSR), the WindSat polarimetric radiometer, or the Special Sensor Microwave Imager Sounder (SSMIS), these model functions have subsequently undergone several stages of refinement. Based on WindSat TB measurements and wind speeds and directions from NCEP GDAS, a model function for the isotropic as well as the four Stokes parameters of the wind direction signal has been presented in [12].

Special consideration is needed to derive the wind-induced emissivity signal at wind speeds above 20 m/s. The problem is the sparse or nonexistence of reliable wind speed and direction observations at those high wind speeds. Few buoy measurements are available above 15 m/s. Moreover, as we will discuss in more detail in Section II-A, even scatterometer wind speeds measurements are not reliable at high winds. The reason for this is that the geophysical model function (GMF), which relates the backscatter cross section to wind speed and which is the basis for the scatterometer wind speed retrieval is not known *a priori*. In the context of training a radiometer wind retrieval algorithm in storms, [13] determined the wind-induced emissivity at high wind speeds for the WindSat channels from WindSat TB measurements that had been collocated with wind speed and directions from the HRD analysis. The challenge hereby is to remove the effect of the raining atmosphere, as most of the high wind speeds in tropical storms are heavily contaminated by rain.

It is the goal of our work to provide a comprehensive model function of the wind-induced emissivity signal for the whole microwave spectrum between C-band and W-band that is applicable over a large interval of EIA ranging from nadir to about 65° and for wind speeds up to 40 m/s. It should be noted in this context that the resolution and footprint size of typical spaceborne microwave sensors limits the highest wind speed that those instruments can observe in hurricane conditions [13]. The highest wind speed that we have observed so far by resampling the HRD analysis hurricane wind fields to the resolutions of the C-band channels of WindSat and AMSR-E is about 45 m/s. The actual value depends on the resolution of the channels that are used for the wind speed retrievals.

We will base our study on TB measurements from WindSat and the SSM/I F13. The reason for choosing these two sensors is, that up to date, they are the best known calibrated instruments [14]. Other sensors are known to have significant calibration problems due to an emissive antenna (TMI, SSMIS F16, and F17) or an intrusion of solar radiation into the hot load (AMSR, SSMIS F16, and F17). Those calibration problems can make the analysis of the wind-induced emissivity signal more challenging. Though the WindSat instrument does also suffer from a small solar intrusion into the hot load, its size is much smaller than it is the case for AMSR or SSMIS and therefore easier to correct. As we will discuss in detail in Section III, the determination of the wind-induced emissivity signal has to go hand in hand with the absolute calibration of the sensor to the RTM, which consists in an on-orbit adjustment of the antenna pattern coefficients (spillover and cross polarization correction) as well as the effective temperature of the hot load [14]. In addition, the local equatorial crossing times of WindSat and SSM/I F13 are within less than 1 h, which makes a direct comparison and cross-collocation between observations from the two instruments easy.

It is obvious that our analysis can only make an assessment of the wind-induced emissivity in the narrow EIA range that is covered by these two sensors, which lies between 49° and 56°. In order to extent the validity down to nadir observations we will need to ingest information from other measurements and studies, which have analyzed the wind-induced emissivity at low EIA. We will test how well our new model function fits the results of those other studies. One focus will be the comparison with the emissivity measurements of NOAA's Step Frequency Microwave Radiometer (SFMR) that have been performed for C-band frequencies between nadir and 45° EIA in storm conditions [15], [16].

It should be noted that one central assumption we make is that the roughness of the ocean surface only depends on wind and not on any other parameters, such as for example significant wave height or the stage of development of the sea. It is possible that the ocean roughness correlates with those parameters in addition to wind speed, but this is not part of our investigation.

Our paper is intended to serve multiple purposes: First of all, we want to demonstrate the steps that are involved in the derivation of the wind-induced emissivity signal and how it is connected to the absolute calibration of the microwave sensors. Second, we want to validate our new model function and compare it with the results of other studies. Last but not least, this paper is also intended to serve as a reference for providing the details of the forms and coefficient of the various components of the emissivity model function. We believe that

TABLE I
DATA SETS USED IN THIS PAPER. THE TABLE INDICATES THE SOURCES OF TB, ATMOSPHERIC PARAMETERS (COLUMNAR WATER VAPOR AND COLUMNAR LIQUID CLOUD WATER), WIND SPEED, AND WIND DIRECTION

Data Set	TB	Water Vapor Cloud Water	Wind Speed	Wind Direction
WS1	WindSat	WindSat	WindSat	NCEP GDAS
WS2	WindSat	WindSat	QuikSCAT	QuikSCAT
WS3	WindSat	WindSat	HRD	HRD
SS	SSM/I F13	SSM/I F13	QuikSCAT	QuikSCAT

this will be useful for researchers who deal with the ocean surface emissivity at microwave frequencies.

Our paper is organized as follows. In Section II we describe the features of the data sets that we have used in our study and give an overview of the major steps that are involved in determining the wind-induced emissivity model function from TB observations. Section III explains the connection between absolute sensor calibration and determination of the wind-induced emissivity model function and shows how both tasks need to be solved consistently. In Section IV, we state the results for the isotropic part of the model function and discuss its dependence on wind speed, SST, EIA, frequency, and polarization. Section V deals with the treatment of the downwelling atmospheric radiation that is scattered from the ocean surface. This radiation is received by the spaceborne or airborne sensor together with the signal that is emitted from the surface and therefore has to be handled together with the emissivity signal. In Section VI, we present and discuss the results for the four Stokes parameters of the wind direction-dependent part of the emissivity signal. Section VII provides a validation of our model function and gives an assessment of its accuracy. The major tool is a comparison of measured versus computed TB being analyzed as 2-D function of SST and wind speed. Another way to validate the model function is to check the geophysical parameters that are retrieved from the model function, and we provide some examples as well. The special treatment of wind speeds above 20 m/s is discussed in Section VIII, which also includes a comparison of our model function with the C-band SFMR results at high wind speeds. Section IX briefly summarizes our main results and conclusions.

II. STUDY DATA SETS AND ANALYSIS METHOD

A. Collocated Brightness Temperature and Wind Observations

Table I gives an overview of the sources of the various data sets that have been used in our analysis. The basis are TB measurements from both the WindSat and the SSM/I F13 sensor that are collocated over independent measurements of wind speed and direction. We have used measurements from about 20 000 orbital revolutions from both instruments comprising a time interval of over 4 years. The WindSat radiometer (http://www.nrl.navy.mil/WindSat/) [17] is fully polarimetric at 10.7, 18.7, and 37.0 GHz with vertical (v), horizontal (h), $+45^\circ$ $(+)$ and -45° $(-)$ and left (lc) and right (rc) circular polarized channels. At 6.8 GHz and 23.8 GHz, only v- and h-pols are measured. The average EIA are: 53.8° at 6.8 GHz, 50.1° at 10.7 GHz, 55.6° at 18.7 GHz, and 53.2° at 23.8 GHz and 37.0 GHz. The Earth field of view contains observations from both the for and the aft section of the swath. The SSM/I F13 sensor [18] takes v-pol and h-pol observations at 19.35, 37.0, and 85.5 GHz and a v-pol observation only at a the water vapor line 22.235 GHz. The average EIA is 53.1° for all channels, and Earth view observations are taken only during the forward look.

Level 0 radiometer count measurements from both instruments are processed into calibrated Level 2 TB following the basic on-orbit calibration outlined in [12], [14]. We will come back to some of the details of the sensor calibration in Section III. The next step is the resampling of the measurements from separate channels to a common location (Level 2 TB) following the optimum interpolation (OI) method of [19], [20]. This can be done at various resolutions. Finally, ocean environmental products are retrieved from the Level 2 TB using a physical multi-stage regression algorithm [8], [12], [21]. The ocean products that are relevant for our analysis are wind speed W referenced to 10 m above the ocean surface, columnar atmospheric water vapor V, and columnar liquid cloud water L. All three products use the 18.7/19.35–37 GHz channels of either WindSat or SSM/I F13. Their resolution is determined by the 3-dB footprint of the lowest, i.e., the 18.7/19.35 GHz channels, whose average size is about 21 km for WindSat and about 56 km for SSM/I F13.

All data are flagged for contamination from rain and nearby land or sea ice. We also need the surface wind direction φ_W from NCEP GDAS, SST T_S from the Reynolds OI product, and SSS S from the climatology from the World Ocean Atlas (WOA98, N.O.D.C., CD-ROM). This comprises the data set WS1 from Table I.

The retrieval algorithms are physical algorithms, that means they are trained with simulated TB that have been calculated from a radiative transfer model (RTM) with realistic ocean-atmosphere scenes. The wind-induced emissivity model is of course part of this RTM. The ocean products that are used in our analysis are retrieved with an algorithm that has been trained with a prior version of the wind-induced emissivity model.

Fig. 1 shows schematically the connection between development of the RTM, calibration of the radiometer, which we will discuss in more detail in Section III, and the retrieval of geophysical products. Once a geophysical parameter has been validated against ground truth *in situ* observations, it becomes ground truth itself and can be used in further development of the RTM, validation, or the calibration of a different sensor. After several stages, the method leads ideally to a stage of self-consistency in which both the RTM as well as the geophysical parameters remain effectively unchanged from the prior step. This reflects the successive refinement of the model development mentioned in Section I. Our wind-induced emissivity model and the wind speeds that are retrieved from it are very close to this stage of self-consistency. This is evident in the small changes of the emissivity model that have occurred from previous versions [9], [11], [12] compared with the model

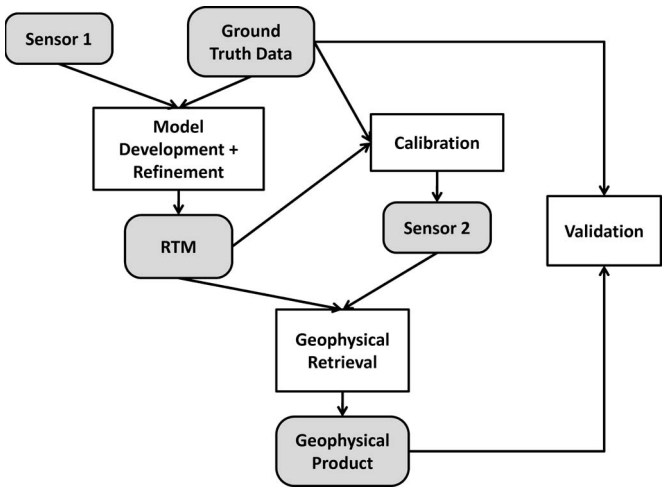

Fig. 1. Schematic flow of model function development, calibration, and validation.

function that will be presented in this paper. Validations of surface wind speeds and directions that were derived from those previous versions can be found in [8], [12], [23], and [24].

We also want to present validation results in our study which uses wind speeds that do not come from a radiometer measurement but have been obtained independently and were collocated with the radiometer TB observation. A good candidate is the NASA scatterometer QuikSCAT, which measures both wind speed and wind direction from the radar backscatter. The ascending node time of QuikSCAT differs from the ascending node times of WindSat and SSM/I F13 by approximately 12 h. Therefore, the descending swaths of QuikSCAT collocate with the ascending swaths of WindSat and SSM/I F13 and vice versa. That means that the majority of collocations take place at lower latitudes. This puts some limitation to the determination of the wind-induced emissivity at very cold SST. Cold SST occur at higher latitudes and are therefore getting undersampled. For creating the sets WS2 and SS in Table I, we have used a time collocation window of 1 h.

What needs to be kept in mind in this context is the fact that scatterometer wind fields are not a given ground truth, but their retrieval is based on a GMF for the radar backscatter [25]. The situation is therefore quite similar to the radiometer wind retrieval which is based on the model function for the wind-induced emissivity. Like the radiometer emissivity model, the scatterometer GMF has undergone several stages of subsequent refinements starting out from using buoy measurements and wind fields from NWP products. An important limitation is the retrieval of high wind speeds from the scatterometer like it is the case for high radiometer wind speeds. No or few reliable ground truth observations exist to determine the scatterometer GMF above 20 m/s.

Our analysis of the wind emissivity at high winds is based on data set WS3 from Table I, which consists of collocations between WindSat TB and HRD wind fields. The method how this set was created is explained in detail in [13]. We will come back to the details of this data set and the wind emissivity and high wind speeds in Section VIII. Note that most observations of set WS3 contain rainy atmospheres.

B. Radiative Transfer Model (RTM) Function

The general RTM expression for the top of the atmosphere (TOA) TB of polarization $p = v, h, +, -, lc, rc$ is:

$$\begin{aligned} T_{B,p} &= T_{BU} + \tau \cdot E_p \cdot T_S + \tau \cdot T_{B\Omega} \\ T_{B\Omega} &= R_p \cdot [T_{BD} + \tau \cdot T_{cold}] + T_{B,scat,p}. \end{aligned} \tag{1}$$

Here, T_S denotes the SST, E_p the total sea surface emissivity, $R_p = 1 - E_p$ the sea surface reflectivity, τ the atmospheric transmittance, T_{BU} the upwelling atmospheric brightness temperature, and T_{BD} the downwelling atmospheric brightness temperature that is reflected at the ocean surface. $T_{B\Omega}$ is the downwelling sky radiation that is scattered from the ocean surface, and T_{cold} is the effective cold space temperature after taking into account the deviation from the Rayleigh-Jeans approximation [14]. The term $\tau \cdot T_{B,scat,p}$ accounts for the atmospheric path length correction in the downwelling scattered sky radiation. We will examine this part and explain how we deal with it in more detail in Section V.

For atmospheres without rain where scattering can be neglected, the atmospheric parts τ, T_{BU}, and T_{BD} can be calculated from the atmospheric profiles of temperature $T(s)$ and the absorption coefficient $\alpha(s)$

$$\begin{aligned} T_{BU} &= \int_0^{TOA} ds \alpha(s) T(s) \tau(s, TOA) \\ T_{BD} &= \int_0^{TOA} ds \alpha(s) T(s) \tau(0, s) \\ \tau(s_1, s_2) &= \exp\left[-\int_{s_1}^{s_2} ds \alpha(s) \right]. \end{aligned} \tag{2}$$

In (2), s is the path length along the propagation of the electromagnetic ray with $s = 0$ being the ocean surface and $s = TOA$ the TOA. The total transmittance is $\tau \equiv \tau(0, TOA)$. We will use a 1-dimensional RTM, which means that the atmospheric temperature is assumed to be horizontally uniform and depends only on the altitude h above the surface. The transformation between s and h in the integrals of (2) is

$$\frac{\partial s}{\partial h} = \frac{1 + \delta}{\sqrt{\cos^2 \theta_i + \delta(2 + \delta)}} \tag{3}$$

where θ_i is the EIA, $\delta = h/R_E$, and R_E is the radius of the Earth. For the cases we are considering, an excellent approximation is to set

$$\frac{\partial s}{\partial h} \approx \frac{1}{\cos(\theta_i)}. \tag{4}$$

C. Determination of the Ocean Surface Emissivity

The surface emissivity E in (1) has three components:

$$E = E_0 + \Delta E_W + \Delta E_\varphi. \tag{5}$$

The emissivity of the specular ocean surface E_0 is by far the largest part. It depends on f, θ_i, T_S, and S and is related to

the complex dielectric constant of sea water ε by means of the Fresnel equations:

$$\begin{aligned} E_{0p} &= 1 - |r_p|^2, \quad p = v, h \\ r_v &= \frac{\varepsilon\cos(\theta_i) - \sqrt{\varepsilon - \sin^2(\theta_i)}}{\varepsilon\cos(\theta_i) + \sqrt{\varepsilon - \sin^2(\theta_i)}} \\ r_h &= \frac{\cos(\theta_i) - \sqrt{\varepsilon - \sin^2(\theta_i)}}{\cos(\theta_i) + \sqrt{\varepsilon - \sin^2(\theta_i)}}. \end{aligned} \tag{6}$$

In [26], a fit for ε was provided based on modeling the frequency dependence through a double Debye relaxation law. An ensemble of weighted data from laboratory measurements and SSM/I observations was used in order to fit the Debye relaxation parameters by minimizing the total error between observations and model. In the course of this study, we have decided to make a small adjustment to the temperature and salinity dependence of some of the Debye parameters of [26] in order to improve the match between measured and modeled TB as function of SST. The updated Debye coefficients summarized in Appendix A. We will analyze the differences between measured and computed TB in more detail in Section VII.

The main focus of this study are the second and the third term in (5): the isotropic wind-induced emissivity $\Delta E_W(W)$, which depends on wind speed W, and the four Stokes parameters of the wind direction signal $\Delta E_\varphi(W, \varphi)$, which contains the dependence on wind direction φ relative to the azimuthal look. Both quantities depend also on f and θ_i. As we will discuss shortly, $\Delta E_W(W)$ also has a small residual dependence on T_S and S. As we will discuss in Section V, our model function for $\Delta E_W(W)$ also depends on the assumption for the atmospheric path length correction of the scattered downwelling atmospheric radiation.

Given the values of the atmospheric parameters τ, T_{BU}, and T_{BD}, the emissivity E can be determined from the measured Level 2 TB by solving the RTM (1) for E. Subtracting the value of the specular emissivity E_0 determines the sum ΔE_W and ΔE_φ. As a first step, we sum over all possible wind directions. Because the large data sets provide global coverage and therefore contain a nearly uniform distribution of all possible values of the relative wind direction φ, the contribution from ΔE_φ drops out, as ΔE_φ is a harmonic function of φ. This determines the isotropic part ΔE_W, which can be binned and analyzed as a function of W and T_S. Once ΔE_W is known, we repeat the whole procedure but this time bin and analyze the residuum $E - (E_0 + \Delta E_W)$ as function of φ and W, which determines the functional form of ΔE_φ.

D. Atmospheric Absorption

For the microwave frequencies under consideration, the atmospheric absorption coefficient has three contributions:

$$\alpha = \alpha_L + \alpha_V + \alpha_O. \tag{7}$$

The liquid cloud water absorption profile α_L depends on atmospheric temperature and liquid cloud water density ρ_L (in grams per cubic centimeter). For nonraining atmospheres, it can be treated using Rayleigh approximation:

$$\alpha_L \approx \frac{6\pi \cdot \rho_L}{\lambda \cdot \rho_0} \cdot \mathrm{Im}\left(\frac{1 - \varepsilon_L}{2 + \varepsilon_L}\right) \tag{8}$$

where $\lambda = c/f$ is the radiation wavelength (in centimeters) and $\rho_0 \approx 1.0$ g/cm^3 is the density of water. ε_L is the dielectric constant of pure (cloud) water, which depends on the radiation frequency f and the cloud temperature T. For its computation, we use dielectric model of [26]. Note, that the high-frequency channels 37.0 and 85.5 GHz are very sensitive to the value of the liquid cloud water content. For typical ocean-atmosphere scenes, an error in the total columnar integral L of 0.01 mm $=$ 10 g/cm^2 leads to an error in the 37.0/85.5 GHz h-pol TB of about 0.9 K/1.3 K. The errors in the v-pol TB are about half that size. In order to minimize possible errors in the high-frequency TB due to uncertainties in the value of L, we have included only measurements where $L < 0.08$ mm when deriving the isotropic emissivity and $L < 0.05$ mm when deriving the wind direction signal.

α_V is the profile of the water vapor absorption and depends on frequency f and the atmospheric temperature T, pressure P, and moisture (water vapor density) ρ_V. The oxygen absorption profile α_O depends on f, T, and P. Our computations are based on the water vapor absorption model of [27] and P. Rosenkranz's FORTRAN code O2ABS.FOR, which itself is based on the O_2 absorption model of [28] and [29]. We have found it necessary to make some adjustments in the atmospheric absorption models in order to match the observed and calculated TB. The most noticeable are changing the strengths of the foreign and self-broadened H_2O continua which is consistent with the findings in [30]. We have also adjusted the temperature coefficient of the nonresonant O_2 continuum based on observations with the WindSat 6.8 and 10.7 GHz channels, where this contribution becomes dominant. More details of our H_2O and O_2 absorption models including a validation study of our WindSat and SSM/I water vapor products will be the subject of a separate publication.

The computation of the atmospheric parts τ, T_{BU}, and T_{BD} of the RTM function (1) can be done in different ways. The most accurate but also most computation intensive method is to use atmospheric profiles for T, P, ρ_v, and ρ_L, scale both ρ_V and ρ_L by the values of the total columnar integrals V and L, respectively and then perform the numerical integrals in (2). A simplified approach, which was demonstrated in [9], is to take typical ocean-atmosphere scenes derive analytic expressions for τ, T_{BU}, and T_{BD} as function of T_S and the columnar values V and L, that were retrieved from the Level 2 TB. This avoids having to compute the full atmospheric integrals (2) for each observations. Finally, it is also possible to derive directly regression formulas for τ, T_{BU}, and T_{BD} from the Level 2 TB without taking the detour of retrieving V and L. This approach was used in [13] and is the preferred method if the atmosphere contains rain as it is the case for set WS3. We have checked that for a large enough data set that contains at least 1 year of satellite observation, all three methods lead to the same final result for the wind-induced emissivity.

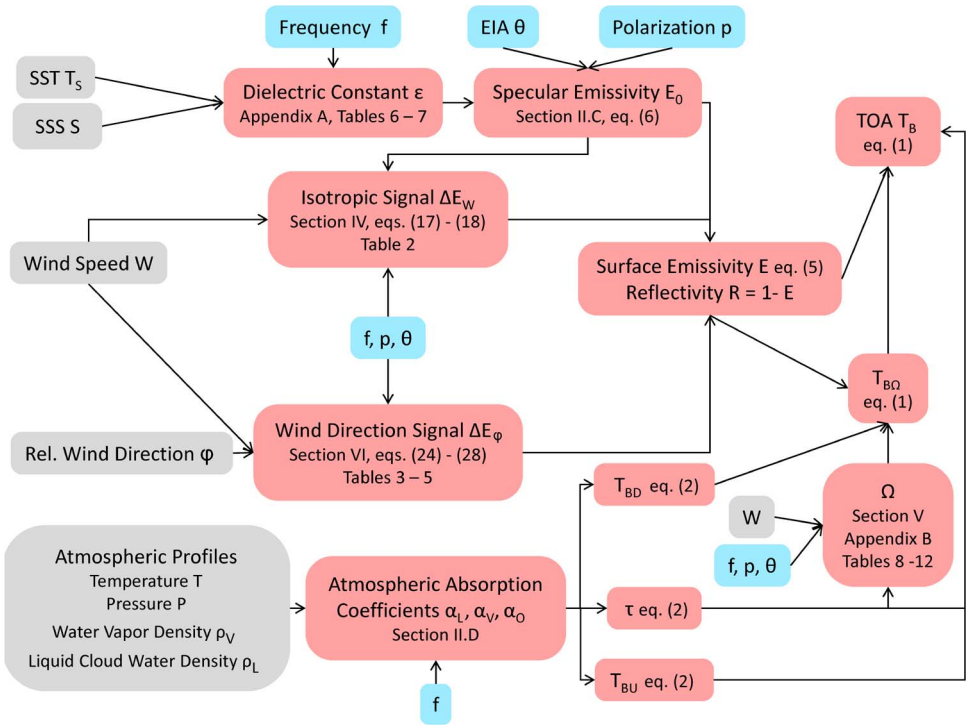

Fig. 2. Schematic flow of the implementation of the various RTM components.

Finally, we need to mention a general issue that arises when retrieving atmospheric parameters from Level 2 TB and using them in the computation of the surface emissivity. The retrieved atmospheric parameters have an error, which leads to an error in the computed emissivity. A pure random error, even if it was large, does not pose a principal problem, as long as the data set that is used in the analysis is large enough. However, if there is any systematic error of the atmospheric parameters that is correlated with wind speed or wind direction, then this error will get backfolded into the computed emissivity, which can lead to a spurious emissivity signal. It is therefore necessary to ensure that there is no significant crosstalk between the retrieved atmospheric product and either W or φ. The fact that both the RTM and the environmental products that we use in our study have undergone several stages of mutual refinement ensures that this is indeed the case. It was shown already in [8] that the satellite derived V and L are basically free from crosstalk with respect to W. In case of the wind direction signal ΔE_φ, the method employed in [10] guaranteed that the errors of the atmospheric parameters are uncorrelated with W and φ. For determining ΔE_φ this is particularly important, because, as shown in [10], even a very small error in the atmosphere can completely swamp the tiny wind direction emissivity signal.

Fig. 2 gives a schematic overview of the implementation of the various components of the RTM, the necessary geophysical and instrument input parameters, and also lists the location in our paper that deals with their computation.

III. Absolute Calibration of Microwave Radiometers

Before discussing the details of the wind emissivity model function, we need to address the role of the absolute sensor calibration in its development. The basic quantity that is measured by a microwave radiometer is receiver counts. The calibration process relates those counts to Level 2 TOA TB and is basically a two-step process [14]. We explain the basic procedure for the simplest case and consider a dual polarization measurement (v-pol and h-pol) at a given frequency.

1) The radiometer counts of the Earth field of view are turned into antenna temperatures (TA). For externally calibrated sensors, two external targets of known temperatures are used as reference. If C_{cold} are the counts measured at the effective cold space temperature T_{cold} and C_{hot}, the counts measured from the hot load at temperature T_{hot}, and if the receiver response is linear, then the TA T_A for an Earth view count C_E is given by

$$T_{A,P} = T_{hot} + \lambda(C_{Earth,p}) \cdot (T_{cold} - T_{hot}), \quad p = v, h \quad (9)$$

where $\lambda(C) \equiv (C - C_{hot})/(C_{cold} - C_{hot})$.

2) The second step is the antenna pattern correction (APC), which turns the TA into TOA TB correcting for cross polarization contamination and spillover, which is the intrusion of cold space into the earth view section. A spillover factor η_p, $p = v, h$, and cross polarization contaminations a_{vh}, a_{hv} between v-pol and h-pol result in a linear transformation between TA and TB:

$$\begin{pmatrix} \tilde{T}_{A,v} \\ \tilde{T}_{A,h} \end{pmatrix} = \mathbf{A} \cdot \begin{pmatrix} T_{B,v} \\ T_{B,h} \end{pmatrix} = \begin{pmatrix} 1 - a_{vh} & a_{vh} \\ a_{hv} & 1 - a_{hv} \end{pmatrix} \cdot \begin{pmatrix} T_{B,v} \\ T_{B,h} \end{pmatrix}$$

$$T_{A,p} = \eta_p \cdot \tilde{T}^{A,p} + (1 - \eta_p) \cdot T_{cold}, \quad p = v, h \quad (10)$$

Ideally, the calibration parameters $T_{hot}, T_{cold}, \eta_v, \eta_h, a_{vh}, a_{hv}$ are known. This would allow one to carry out the transformation

(9) from counts to TA and then from TA to TOA TB, which is the inversion of (10). Unfortunately, experience with all known spaceborne microwave sensors shows that most of these parameters cannot be measured accurately enough in order to obtain the required precision for the TB. This has various reasons. Gradients within the hot load, which can be caused or at least enhanced by intrusion of solar radiation result in an inaccurate determination of T_{hot} from the temperature readings of the hot load thermistors. Prelaunch determination of the APC is difficult, particularly an accurate determination of the spillover coefficients, as it requires an accurate knowledge of the antenna patterns over the whole backlobes of the main reflector. Absolute radiometer calibration consists in determining effective values for the calibration parameters by matching observed TOA TB from ocean scenes to TB that were calculated from an accurate RTM. This is done in an average sense using a large data set that contains at least several months of observations. We assume that the effective cold space temperature T_{cold} is known exactly. We also assume that $\eta_v = \eta_h \equiv \eta$ and $a_{vh} = a_v \equiv a$. For most known antenna patterns, there is excellent symmetry in the v-pol and h-pol ports. The observation $T_{B,v} = T_{B,h}$ over hot densely vegetated land scenes also confirms that $\eta_v = \eta_h$ to high degree of accuracy. If T_{cold} is small compared to T_{hot} and both $1-\eta$ and a are small compared to 1, then the count to TOA TB transformation reads up to first order in these small parameters:

$$T_{B,p} \approx \frac{T_{hot}}{\eta} + \lambda(C_{Earth,p}) \cdot \left[T_{cold} - \frac{T_{hot}}{\eta}\right] - a \cdot \frac{T_{hot}}{\eta} \cdot [\lambda(C_{Earth,p}) - \lambda(C_{Earth,x})] + \cdots. \quad (11)$$

The symbol $x = h, v$ denotes the cross polarization to $p = v, h$. The Earth view counts $C_{Earth,p}$ are measured by the sensor. The TOA TB $T_{B,p}$ are computed from the RTM. If this is done for an average of a large data set of ocean scenes, one can use environmental parameters from a NWP model or even a climatology for doing that. It is then possible to solve the calibration conditions in (11) for the two unknown parameters, namely T_{hot}/η and a. It is therefore possible to make either an adjustment of prelaunch value for the spillover η or add a constant overall bias to the on-orbit measurement of the hot-load temperature T_h, so that the measured T_B matches the computed T_B. Once T_{hot}/η and a have been fixed that way, their values are used subsequently when transforming counts into TA. This procedure defines the *absolute calibration of the radiometer to an ocean RTM*. It should be noted, that only the ratio T_{hot}/η of the effective hot load temperature and spillover is entering into (11). The absolute calibration cannot determine separate values for T_{hot} and η. In order to do that some additional information would be necessary. For example, if it is known that at certain times the hot load is free from solar intrusion and gradients and therefore T_{hot} is accurately given by its thermistor readings, then η itself can be determined.

We now turn to the role of absolute calibration in determining the wind-induced emissivity model from TOA TB. These TOA TB need to be absolutely calibrated to an ocean RTM and the emissivity model that is to be determined is itself part of this ocean RTM. Therefore, both problems need to be dealt with together and solved self-consistently. The standard way is to start out with a good first guess for the calibration parameters (T_h, η, a) and then determine the wind-induced emissivity as described in Section II-C. The crucial step consists then in analyzing the isotropic wind-induced emissivity $\Delta E_W(W)$ for very low wind speeds, say between 0 and 3.5 m/s. The central assumption is that at low wind speeds, $\Delta E_W(W)$ is proportional to W and in particular that $\Delta E_W(W=0) = 0$. When looking at the actual data, one will find that this is in general not the case. Performing a linear fit of $\Delta E_W(W)$ to W at very low wind speeds results in

$$\Delta E_W(W) \approx \delta_0 + \delta_1 \cdot W \quad (12)$$

with a finite offset δ_0. This can have various reasons. It might be a residual inaccuracy in one of the other components of the RTM, such as the dielectric constant of sea water or the atmospheric absorption. Assuming that we have validated those other components, then the most likely reason for a finite offset δ_0 is that is that the first guesses for the calibration parameters were not accurate enough. The better this first guess was, the smaller the value for δ_0. We demand that the low wind speed behavior is given for both v-pol and h-pol by

$$\Delta E_W(W) \approx \delta_1 \cdot W \quad (13)$$

instead of (12) and perform an absolute calibration of the TOA TB to the RTM with the emissivity model function (13) using only low wind speeds. We have visualized this process in the right panel of Fig. 3 showing the linear fit to the low wind speed region of data set WS1 at 6.8 GHz (red squares) for wind speeds between 0 an 3.5 m/s as dashed lines. The emissivity model function, which is obtained in this way, does then fulfill the desired constraint $\Delta E_W(W) = 0$. Once we have determined the calibration parameters from TB observations at low wind speeds, we assume that they can be applied universally, which then allows us to determine $\Delta E_W(W)$ over the whole wind speed region. As a check of self-consistency, we perform the absolute calibration a second time using now TB measurements at all wind speeds with the full $\Delta E_W(W)$ model function. We find that the calibration parameters that are found in this second step have changed only very little compared with the values from the absolute calibration at low wind speeds, the radiometric impact of the change being in the order of 0.1–0.2 K. This is within the required level of accuracy of the calibrated TB. This demonstrates that we have reached closure in the self-consistent determination of the wind emissivity model function from TB that are absolutely calibrated to an ocean RTM containing this same emissivity model function.

On a final note, we want to emphasize that it is essential to use exactly the same RTM for performing the absolute calibration and training the physical retrieval algorithm of the environmental parameters mentioned in Section II-A. Otherwise, it is very likely that the retrieved environmental parameters exhibit biases when compared to ground truth measurements.

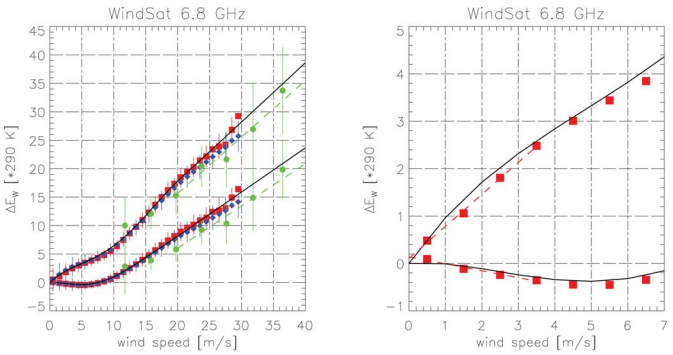

Fig. 3. Wind-induced ocean surface emissivity near the reference temperature $T_{ref} = 20$ °C for the 6.8 GHz v-pol (lower curves) and h-pol (upper curves) channels at EIA 53.8 ° from WindSat TB measurements. The solid lines are the model functions from Section IV of this paper. The red squares/blue diamonds are the results from the analysis of set WS1/set WS2 of Table I, if WindSat (QuikScat) wind speeds are used for binning. For clarity, only every second error bar is displayed. The green circles in the left panel are the results from [13] using HRD wind speeds (set WS3 from Table I). The dashed lines are linear fits to these data above 20 m/s. The right panel magnifies the low wind speed region of data set WS1. The red dashed lines in the right panel are the linear fits to the red squares in the wind sped interval 0–3.5 m/s. The emissivities have been multiplied by a typical surface temperature of 290 K.

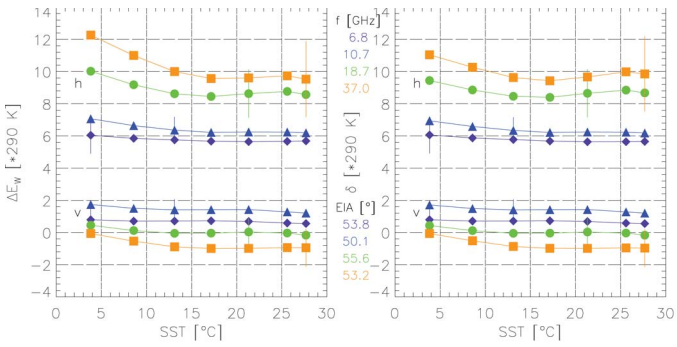

Fig. 4. Wind-induced ocean surface emissivities $\Delta E_W(T_S)$ (left panel) and values of the expression $(\Delta E_W(T_S)/E_0(T_S)) \cdot \Delta E_W(T_{ref})$ (right panel) for WindSat channels from data set WS2 as function of SST T_S within the wind speed interval 9.0–10.0 m/s. The emissivities have been multiplied by a typical surface temperature of 290 K. The lower curves are for v-pol, and the upper curves are for h-pol.

IV. Isotropic Emissivity Signal

A. Dependence of the Wind-Induced Ocean Surface Emissivity on Wind

Fig. 3 shows ΔE_W for the WindSat 6.8 GHz v-pol and h-pol channels. The average EIA is 53.8°. The SST has been restricted to lie within ±2 K of the reference SST $T_{ref} =$ 20 °C. We will study the SST and EIA dependence of the wind-induced emissivity in the next two sections. The red squares/blue diamonds indicate the results from sets WS1/WS2, which are using WindSat/QuikSCAT wind speeds. There is excellent agreement between the two data sets up to 20 m/s within the margins of error. For the reasons spelled out in Section II-A, we do not use QuikSCAT wind speeds and data set WS2 for determining the emissivity curve above 20 m/s but rather will reside to set WS3 and wind speeds form the HRD analysis, which are the green circles in Fig. 3. The details of the high wind speed fit will be explained in Section VIII.

In order to obtain a functional dependence of $\delta^i(W)$, we average the values for ΔE_W^i restricted to the SST interval $T_{ref} \pm 1$ K into discrete wind speed bins of 0.5 m/s size. For all channels i, the wind speed dependence of ΔE_W up to 20 m/s for both v-pol and h-pol can be accurately fitted by a fifth-order polynomial

$$\Delta E_W^i(W, T_{ref}) = \delta^i(W) = \sum_{k=1}^{5} \delta_k^i \cdot W^k \qquad (14)$$

which is the black curve in Fig. 3. The channel i is characterized by frequency f, polarization p and EIA θ. The offset δ_0 in (12) has been calibrated to zero, as explained in Section III. As we will discuss in Section VIII, the wind emissivity function $\Delta E_W^i(W, T_{ref}) = \delta^i(W)$ keeps increasing linearly with W above 20 m/s.

B. Dependence of the Wind-Induced Ocean Surface Emissivity on Sea Surface Temperature

It has been already observed by [9] and [12], that the wind-induced emissivity has a residual SST dependence. ΔE_W is slightly larger in cold water than in warm water. The left panel of Fig. 4 shows that for the channels of the set WS2 in Table I, the dependence of ΔE_W on T_S resembles very closely the dependence of the specular emissivity E_0 on T_S. This behavior is not unexpected. The wind roughened surface mixes the vertical and horizontal polarizations of the specular surface, and the mixing increases with increasing emissivity of the specular surface. The data analysis suggests for the channels covered by the sets of Table I the dependence of ΔE_W on W and T_S can be modeled by

$$\Delta E_W^i(W, T_S, S) = \delta^i(W) \cdot \frac{E_0^i(T_S, S)}{E_0^i(T_{ref}, S)}. \qquad (15)$$

The wind speed dependence $\delta^i(W)$ is given by (14). The right panel of Fig. 4 shows the value of $\delta_i(W)$ from (15). Ideally, if (15) was holding exactly, the curves in the right panel of Fig. 4 would be flat. The figure shows that, though not perfect, (15) provides an adequate parameterization of the T_S dependence of $\Delta E_W(W, T_S)$. Using this parameterization allows to eliminate effectively one degree of freedom in the two-dimensional fit of $\Delta E_W(W, T_S)$.

C. Dependence of the Wind-Induced Ocean Surface Emissivity on Earth Incidence Angle

The difference in the EIA of the 18.7/19.3 GHz channels of WindSat (55.6°) and SSM/I (53.1°) allows our analysis to make a limited direct assessment of the EIA dependence of ΔE_W within that EIA range. Fig. 5 shows ΔE_W from data sets WS2 and SS over EIA for two different wind speeds. Our results indicate a weak increase of ΔE_W^h and a noticeable decrease of ΔE_W^v with increasing EIA.

Our analysis is obviously not able to directly determine the functional behavior of ΔE_W on the EIA θ_i outside the range that is covered by the study data sets. In order to develop a model function that is valid for all θ_i, we need to ingest results

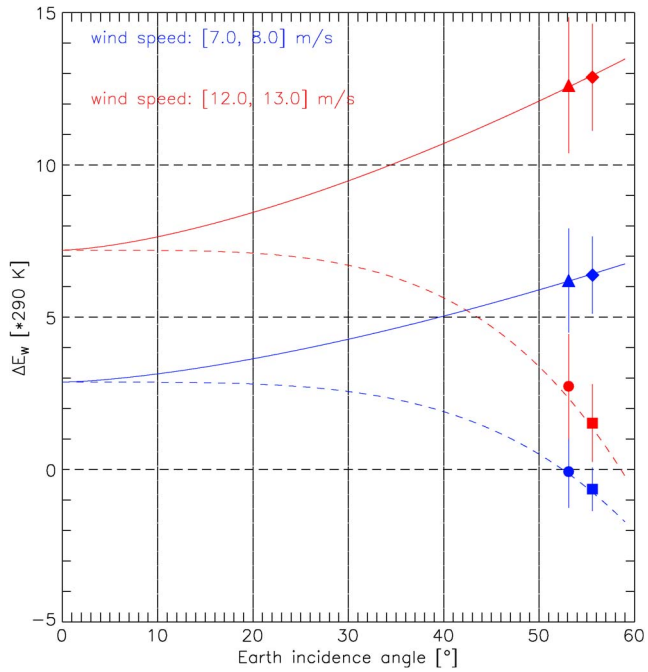

Fig. 5. Wind-induced ocean surface emissivity near the reference surface temperature $T_{ref} = 20$ °C as function of the EIA for two wind speed intervals. The data are the results from the analysis of sets WS2 and SS from Table I (squares = WindSat v-pol, diamonds = WindSat h-pol, circles = SSM/I v-pol, triangles = SSM/I h-pol). The curves are the functional fits from Section IV-C (dashed = v-pol, dash-dot-dot = h-pol). The emissivities have been multiplied by a typical surface temperature of 290 K.

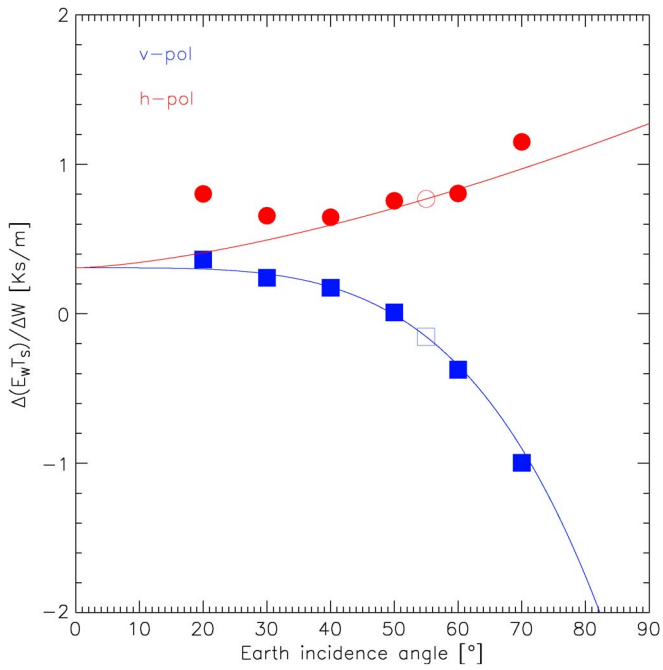

Fig. 6. Slope of the wind-induced ocean surface emissivity with wind speed $\Delta(E_W \cdot T_S)/\Delta W$ from [18] as function of EIA. The filled symbols are the measurements from [18] after subtracting the contribution of the atmospheric downwelling reflected radiation. The open symbols indicate the values after interpolating to the reference EIA $\theta_{ref} = 55.2°$. The full lines are the results of our fit function (16) after setting the v-pol and h-pol emissivities at $\theta_{ref} = 55.2°$ to the values indicated by the open symbols.

from other measurements. At nadir, both ΔE_W^v and ΔE_W^h have the same value ΔE_W^{nad}. The results from [31] and [32] suggest that ΔE_W^{nad} is approximately given by the arithmetic average of the v-pol and h-pol values at around 55° and that the EIA dependence of ΔE_W can be parameterized by a low/high order polynomial in θ_i for h-pol/v-pol. It should be noted in this context that the observation platform measurements of [18] only include wind speeds below 15 m/s with no foam-covered sea surfaces. The data presented in [31] and [32] refer to TB rather than surface emissivity. Therefore, a correction for atmospheric effects needs to be done in order to obtain values for the emissivity. No measurements below $\theta_i = 20°$ could be performed in [31], because the observation tower entered the field of view. Our analytic form of ΔE_W reads

$$\begin{aligned}\Delta E_W^{p,f}(\theta_i, W, T_S, S) = {} & \Delta E_W^{nad,f}(W, T_S, S) \\ & + \Big[\Delta E_W^{p,f}(\theta_{ref}, W, T_S, S) \\ & - \Delta E_W^{nad,f}(W, T_S, S)\Big] \cdot \left(\frac{\theta_i}{\theta_{ref}}\right)^{x_p} \\ \Delta E_W^{nad,f}(W, T_S, S) = {} & \frac{1}{2}\Big[\Delta E_W^{v,f}(\theta_{ref}, W, T_S, S) \\ & + \Delta E_W^{h,f}(\theta_{ref}, W, T_S, S)\Big]. \end{aligned} \quad (16)$$

For the exponents x_p, $p = v, h$ we choose $x_v = 4.0$ and $x_h = 1.5$ at all frequencies and wind speeds. The form (16) applies for $\theta_i \le \theta_{ref}$. We linearly extrapolate the θ-dependence for $\theta_i \ge \theta_{ref}$.

To compare our EIA dependence with the results of [18], we show the slope of the wind-induced ocean surface emissivity with wind speed $\Delta(E_W \cdot T_S)/\Delta W$ from [18] as function of EIA in Fig. 6. The filled symbols are the measurements from [18] after subtracting the contribution of the atmospheric downwelling reflected radiation. The open symbols indicate the values after interpolating to the reference EIA $\theta_{ref} = 55.2°$. The full lines are the results of our fit function (16) after setting the v-pol and h-pol emissivities at $\theta_{ref} = 55.2°$ to the values indicated by the open symbols. This demonstrates that the functional form given by (16) describes the EIA dependence of ΔE_W well between 25° and 70°. Due to the lack of measurements above 15 m/s, considerable uncertainty exists for the case of high wind speeds and very low EIA.

The emissivity at the reference EIA $\theta_{ref} = 55.2°$ is given according to (15)

$$\Delta E_W^{p,f}(\theta_{ref}, W, T_S, S) = \delta_{ref}^{p,f}(W) \cdot \frac{E_0^{p,f}(\theta_{ref}, T_S, S)}{E_0^{p,f}(\theta_{ref}, T_{ref}, S)} \quad (17)$$

$\delta_{ref}^{p,f}(W)$ is the emissivity for polarization p and frequency f at reference EIA θ_{ref} and the reference SST T_{ref} and is fitted by the fifth-order polynomial (14)

$$\delta_{ref}^{p,f}(W) = \sum_{k=1}^{5} \delta_k^{p,f} \cdot W^k. \quad (18)$$

The coefficients $\delta_k^{p,f}$, $k = 1, \ldots 5$ are listed in Table II for both polarizations p and a selected set of reference frequencies f. Here, as in the following, the wind speed W is always measured in m/s. Linear interpolation can be used to compute $\delta_{ref}^{p,f}$

TABLE II
COEFFICIENTS δ_k, $k = 1, \ldots 5$ IN (18)

f [GHz]	p	1	2	3	4	5
6.8	v	4.96726E-05	-3.03363E-04	5.60506E-05	-2.86408E-06	4.88803E-08
6.8	h	3.85750E-03	-5.10844E-04	4.89469E-05	-1.50552E-06	1.20306E-08
10.7	v	-2.35464E-04	-2.76866E-04	5.73583E-05	-2.94364E-06	4.89421E-08
10.7	h	4.17650E-03	-6.20751E-04	6.82607E-05	-2.47982E-06	2.80155E-08
18.7	v	3.26502E-05	-3.65935E-04	6.62807E-05	-3.40705E-06	5.81231E-08
18.7	h	5.06330E-03	-7.41324E-04	8.54446E-05	-3.28225E-06	4.01950E-08
37.0	v	-7.03594E-04	-2.17673E-04	4.00659E-05	-1.84769E-06	2.76830E-08
37.0	h	5.63832E-03	-8.43744E-04	1.06734E-04	-4.61253E-06	6.67315E-08
85.5	v	-3.14175E-03	4.06967E-04	-3.33273E-05	1.26520E-06	-1.67503E-08
85.5	h	6.01311E-03	-7.00158E-04	1.26075E-04	-7.27339E-06	1.35737E-07

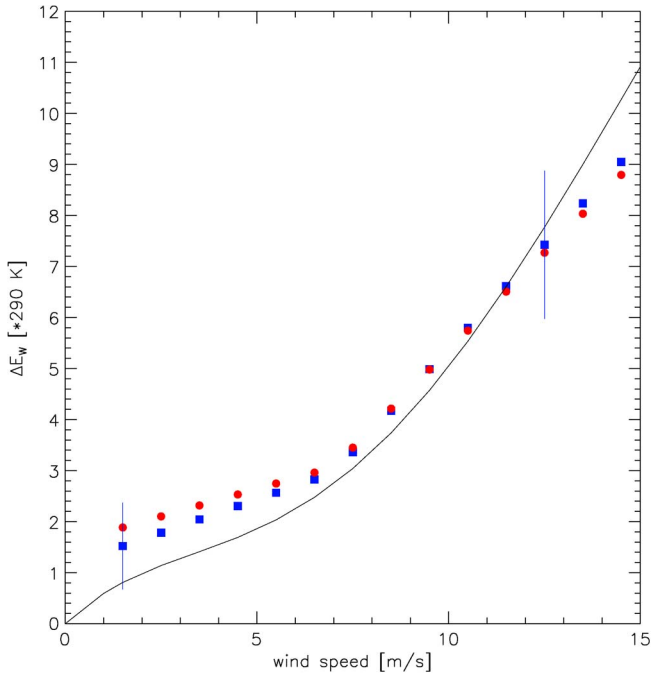

Fig. 7. Comparison of wind-induced ocean surface emissivity from TOPEX/Poseidon [33] and our model as function of wind speed at 18 GHz. The blue squares are the original data from [33]. The red circles are the data after applying a correction for the atmospheric path length correction in the scattered downwelling radiation and referencing the data to our dielectric model. The black curve shows the emissivity model of this paper for $T_S = 15$ °C. Typical error bars are indicated at selected data points. The emissivities have been multiplied by a typical surface temperature of 290 K.

if f lies between the reference frequencies. This completely determines the model function for ΔE_W.

Because of the uncertainties in extending the model function to small EIA, a check with an independent data source is in order. A good one is provided by the emissivity measurements that were performed at nadir and three frequencies (18.0, 21.0, 37.0 GHz) with the TOPEX/Poseidon radiometer [33] using QuikSCAT wind speeds as ground truth. The results for the 18 GHz channel are shown in Fig. 7. The blue squares are the original data from [33]. In [33], no correction for the atmospheric path length correction the in the downwelling reflected radiation (c.f. Section V) was performed, and also a different model for the dielectric constant was used. Applying a correction to the data of [33] that takes both effects into account leads to the red circles in Fig. 7. The black curve displays the emissivity model of this paper for $T_S = 15$ °C at nadir. It agrees with the results of [33] up to 1 K, which lies within the margins of error.

D. Dependence of the Wind-Induced Ocean Surface Emissivity on Frequency

Figs. 8 and 9 examine the spectral signature of ΔE_W. In order to allow an easy comparison, both figures show the values at the reference EIA $\theta_{ref} = 55.2°$. Over the whole frequency range that is covered by our analysis data sets, the h-pol emissivity $\Delta E_W^h(f)$ increases roughly linearly with the logarithm of the frequency $\log(f)$. The v-pol emissivity $\Delta E_W^v(f)$ show almost no spectral dependence for frequencies between 6.8 and 24 GHz. At higher frequencies, $\Delta E_W^v(f)$ decreases with increasing frequency and becomes negative at low and moderate wind speeds. Our observation is in qualitative agreement with that of many other studies, e.g., [31] [32] and [34]. In [34], a strong roll-off of the v-pol emissivity was observed frequencies below 6 GHz. The frequency range that is covered by our data sets does not allow us to see this strong roll-off, as our lowest frequency 6.8 GHz lies just at the edge where it starts to happen. However, when comparing the results for 6.8 and 10.7 GHz, Figs. 8 and 9 both clearly indicate that the v-pol emissivity starts decreasing with decreasing frequency at very low frequencies.

Finally, we want to mention that for the 85.5 GHz channels, our new model functions agrees very well with our earlier results [11] at the SSM/I EIA of 53.1°.

V. DOWNWELLING SCATTERED ATMOSPHERIC RADIATION

The electromagnetic radiation coming from the ocean surface consists of two parts.

1) The radiation that is directly emitted from the surface, which is the term $E \cdot T_S$ in the RTM (1).
2) Downwelling sky radiation (atmospheric and cold space) that is scattered at the ocean surface, which is the term $T_{B\Omega}$ in (1).

If the surface is rough, this radiation is scattered from a big range of directions $\theta_s$into the incident direction θ_i. The atmospheric path through which this radiation has travelled differs from the atmospheric path if the reflection came only from the incident direction $\theta_s = \theta_i$. This difference in atmospheric path lengths needs to be taken into account in the RTM. There are different ways to do this. If the Kirchhoff law $R = 1 - E$ is used in (1), a correction needs to be performed, which is formally done in (1) by adding the correction term $\tau \cdot T_{B,scat}$. The $T_{B,scat}$ itself refers to the ocean surface, and the additional factor τ accounts for the radiation traveling to the TOA.

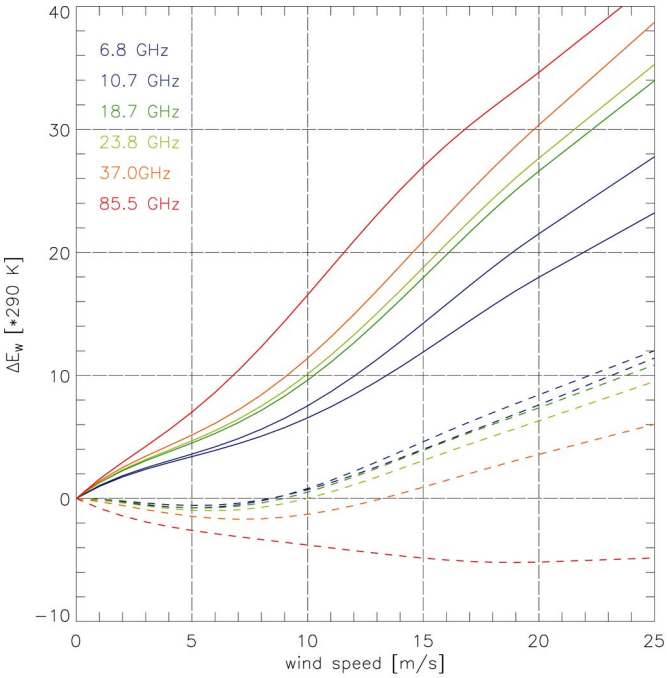

Fig. 8. Model functions from Section IV of this paper for the wind-induced ocean surface emissivity at six different frequencies as function of wind speed. The curves are displayed for the reference surface temperature $T_{ref} = 20$ °C and the reference EIA $\theta_{ref} = 55.2°$. Dashed lines show the v-pol, and solid lines show the h-pol. The emissivities have been multiplied by a typical surface temperature of 290 K.

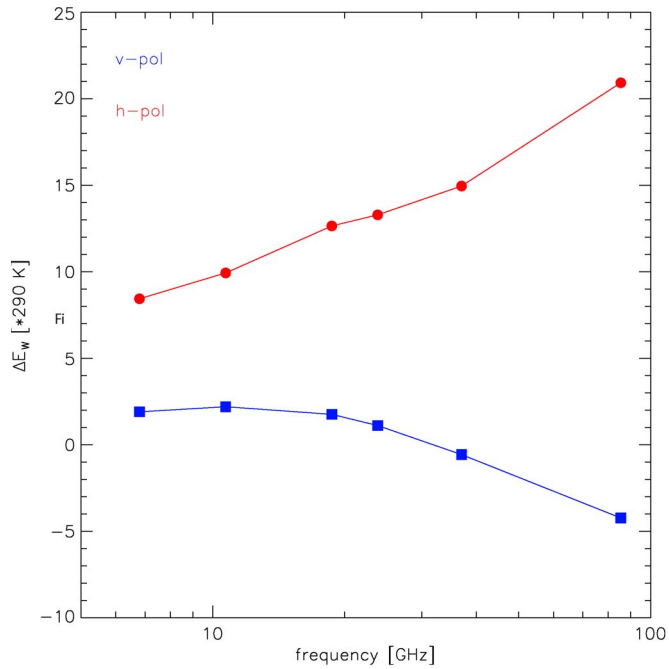

Fig. 9. Spectral dependence of the wind-induced ocean surface emissivity. The figure shows the values of the model function from Section IV of this paper within the wind speed interval 12.0–13.0 m/s at the reference surface temperature $T_{ref} = 20$ °C and at the reference EIA $\theta_{ref} = 55.2°$ as function of the logarithm of the frequency. Blue squares show the v-pol and red circles show the h-pol. The emissivities have been multiplied by a typical surface temperature of 290 K.

The effect can be best understood by writing down R and $T_{B\Omega}$ in terms of the normalized bistatic radar cross

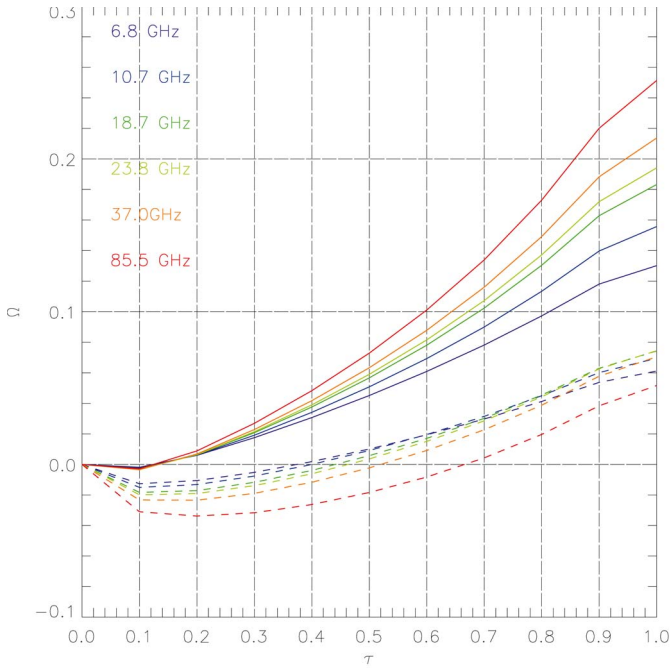

Fig. 10. Model function for the parameter Ω in the atmospheric path length correction (21) as function of the atmospheric transmittance τ at six frequencies. The curves have been computed using $T_S = T_{ref} = 20$ °C, a typical atmospheric temperature of $T_D = T_{BD}/1 - \tau = 281$ K and a wind speed of 7.0 m/s. $\theta_{ref} = 55.2°$. Dashed lines show the v-pol, and solid lines show the h-pol.

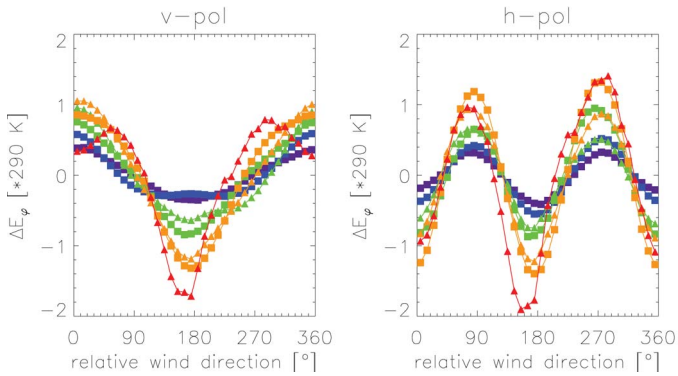

Fig. 11. Wind-directional signal of the ocean surface emissivity as function of relative wind direction for WindSat and SSM/I v-pol and h-pol channels: WindSat 6.8 GHz (purple squares), WindSat 10.7 GHz (blue squares), WindSat 18.7 GHz (green squares), SSM/I 19.3 GHz (green triangles), WindSat 37.0 GHz (orange squares), SSM/I 37.0 GHz (orange triangles), SSM/I 85.5 GHz (red triangles). Wind speed and wind direction were taken from QuikSCAT (sets WS2 and SS from Table I). The wind speed interval is 9.0–10.0 m/s. The emissivities have been multiplied by a typical surface temperature of 290 K.

sections $\sigma(\hat{k}_s, \hat{k}_i)$ [35]

$$R_p(\hat{k}) = \frac{\sec(\theta)}{4\pi} \cdot \int_0^{\pi/2} d\theta_s \sin(\theta_s) \int_0^{2\pi} d\varphi_s \left[\sigma_p(\hat{k}_s,\hat{k}) + \sigma_x(\hat{k}_s,\hat{k})\right]$$

$$T_{B\Omega,p}(\hat{k}) = \frac{\sec(\theta)}{4\pi} \cdot \int_0^{\pi/2} d\theta_s d\theta_s \sin(\theta_s) \int_0^{2\pi} d\varphi_s (T_{BD} + \tau \cdot T_{cold}) \times \left[\sigma_p(\hat{k}_s,\hat{k}) + \sigma_x(\hat{k}_s,\hat{k})\right]. \quad (19)$$

The index x refers to the polarization direction orthogonal to p. $\hat{k}$ and $\hat{k}_s$ are the unit propagation vectors of the incident and scattered radiation, respectively, and are given in terms of the corresponding polar and azimuth angles

$$\hat{k} = (\sin(\theta)\cdot\cos(\varphi), \sin(\theta)\cdot\sin(\varphi), \cos(\theta))$$
$$\hat{k}_s = -(\sin(\theta_s)\cdot\cos(\varphi_s), \sin(\theta_s)\cdot\sin(\varphi_s), \cos(\theta_s)). \quad (20)$$

Both integrals are over the 2π steradian of the upper hemisphere. If the term $(T_{BD} + \tau T_{cold})$ in the second integral of (19) was independent on direction, it could be taken in front of the integral and one would simply recover that $T_{B\Omega} = R\cdot(T_{BD} + \tau\cdot T_{cold})$, i.e., $T_{B,scat}$ would vanish. However, in general, both terms depend on the atmospheric path length according to (3), and therefore a finite correction term $T_{B,scat}$ needs to be added. This is called the atmospheric path length correction. It is typically parameterized as [9]

$$T_{B,scat,p} = \Omega_p(\tau, W)\cdot[T_{BD} + \tau\cdot T_{cold} - T_{cold}]\cdot R \quad (21)$$

where $\Omega_p(\tau, W = 0) = 0$ and $\Omega_p(\tau = 0, W) = 0$. This ansatz automatically guarantees that the $T_{B,scat}$ vanishes for a smooth surface $(W = 0)$ and for a completely opaque $(\tau = 0)$ and a completely transparent ($\tau = 1, T_{BD} = 0$) atmosphere. Opaque and transparent atmospheres are isotropic, and therefore no atmospheric path length correction exists. There are other approaches that account for the atmospheric path length correction by using an effective reflectivity $R_{eff}(\theta_i')$ at an effective incidence angle $\theta_i' \neq \theta_i$ instead of the Kirchhoff law $R(\theta_i) = 1 - E(\theta_i)$ in (1).

It is not possible to separate the effect of $T_{B,scat}$ from the other contribution containing the surface emissivity in the measured TOA TB. If, as in our approach, the emissivity is to be computed from the measured TOA TB, it is therefore necessary to precompute $T_{B,scat}$ based on a surface roughness model. We use the GO model (Kirchhoff approximation) [3], [9] for computing the parameter Ω_p in (21), which characterizes the strength of the atmospheric path length correction. This is done by numerically computing the integrals in (19) and then solving for Ω in (21). As mentioned in Section I, in the GO model, the ocean surface is considered as ensemble of tilted facets each acting individually as an infinitely large specular reflecting surface. We also include the contribution of multiple scattering and shadowing [3]. In contrast to [9], we do not attempt to fit an analytic form to the term $\Omega_p(\tau, W)$ as function of τ and W, as this turns out to be too cumbersome for the whole range of EIA and frequencies that we want to consider in this study. Instead numerical values for Ω_p, $p = v, h$ are precomputed from the GO surface integrals and stored in a large table for representative values of f, θ_i, τ, and W. This table can later be used for fast computation. We want to emphasize that only Ω_p is computed from the GO model. The value for $R_p = 1 - E_p$ is the one that comes from our emissivity model.

One crucial input for the GO model is the variance of the slope distribution $\Delta\Sigma^2(f, W)$ of the tilted facets. It depends on the degree of the surface roughness and therefore on the wind speed W. Each facet with slope Σ is weighted by the Gaussian distributed probability $P(\Sigma)$ with variance $\Delta\Sigma^2(f, W)$. Most studies use the standard value of Cox and Munk [36] for $\Delta\Sigma^2(f, W)$. We have a made a slight adjustment to the Cox–Munk value and use for both polarizations the value

$$\Delta S^2(f, W) = 0.0029\cdot\log_{10}(2f)\cdot\begin{cases} W, & W \le W_0 \\ W_0, & W > W_0. \end{cases} \quad (22)$$

The frequency f is measured in GHz and $W_0 = 20$ m/s. At 37 GHz, the value from (22) is very close to the Cox–Munk expression. The linear increase of the slope variance with the logarithm of the frequency is suggested by the spectral behavior of the h-pol emissivity, which also increases linearly with $\log(f)$, as we have discussed in Section IV-D. Another reason for using (22) is the fact, that the computed values for ΔE_W of the 23.8-GHz channels come out to lie nicely between the values of the 18.7- and 37.0-GHz channels, as it should be. The 23.8 GHz is near the water vapor line and therefore very sensitive to atmospheric effects including the atmospheric path length correction. It is a good indication that the atmospheric path length correction is handled incorrectly, if the emissivity of the 23.8-GHz channels does not end up close to its interpolated value from 18.7 and 37.0 GHz.

Fig. 10 shows the size of Ω for both polarizations $p = v, h$ at the reference EIA $\theta_{ref} = 55.2^\circ$ and a wind speed of 7.5 m/s over the range of frequencies in our data sets. The size of the atmospheric path length correction depends on frequency and the actual value of τ. The dynamical range that τ can take depends itself on frequency. For the low frequency channels, 6.8 and 10.7 GHz, τ stays close to 1 in nonraining atmospheres. For the higher frequency channels, the values of τ can become considerably lower. As it can be read off from Fig. 10, the atmospheric path length correction for the h-pol at the reference EIA $\theta_{ref} = 55.2^\circ$ leads to an increase of the brightness temperature, and the effect grows with growing frequency. For the v-pol, the atmospheric path length correction stays small as the wind-induced emissivity does and can even become slightly negative at small values of τ.

It is important to emphasize that in deriving our emissivity model function, we have used the values for Ω from the GO model with the slope distribution (22) when solving the RTM equation. Therefore, any accurate RTM calculation of the TOA TB that uses the emissivity model from this paper will need to be done using exactly the same atmospheric path length correction. It is possible to use a different, possibly more elaborate approach for the computation of Ω. If that that is done, the value of ΔE_W can also change. In our approach, it is only meaningful to use ΔE_W and Ω together and consistently within the RTM.

Neglecting the atmospheric path length correction completely amounts to substitute the wind-induced emissivity $\Delta E_W(W, \ldots)$ in the RTM (1) with the effective wind-induced emissivity $\Delta E_W^*(\tau, W, \ldots)$, which can be read off from (1)

$$\Delta E_W^*(\tau, W, \ldots) = \Delta E_W(W, \ldots) + \frac{T_{B,scat}(\tau, W, \ldots)}{[T_S - T_{BD} - \tau\cdot T_{cold}]}. \quad (23)$$

The $\ldots$ indicate the dependence on parameters other than W and τ. This effective emissivity would depend on the at-

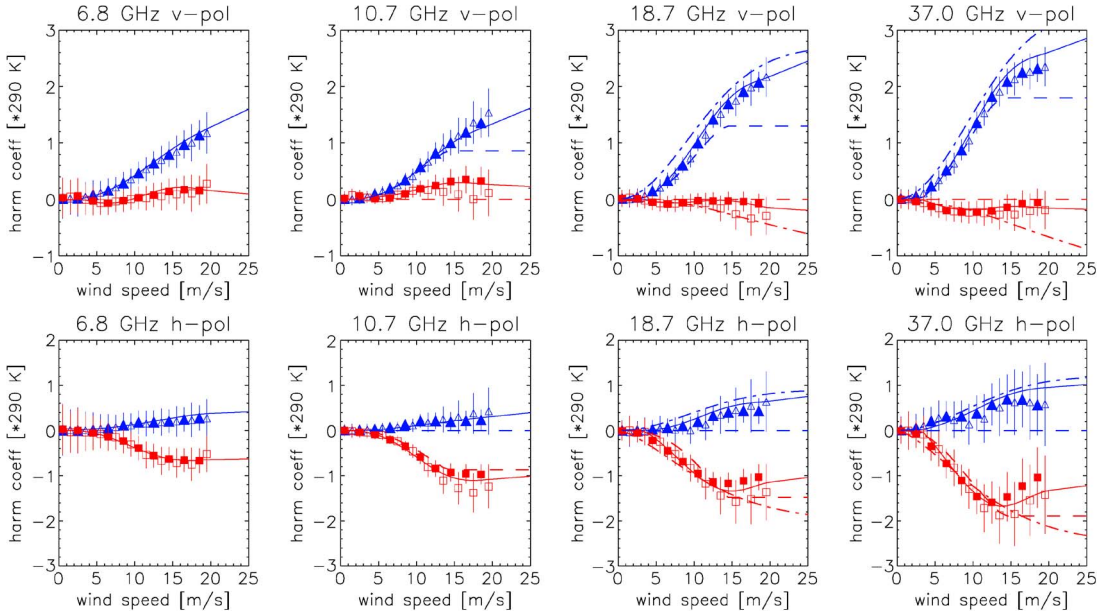

Fig. 12. First (blue) and second (red) harmonic coefficients for WindSat v-pol and h-pol channels as function of wind speed. The filled symbols are the results if WindSat wind speed and NCEP wind direction (set WS1 from Table I) are used. The open symbols are the results if QuikSCAT wind speed and direction (set WS2 from Table I) are used. The solid lines are the model functions from Section VI of this paper. The dashed lines are the results of [10]. The dash-dot lines are the results of [38]. The emissivities have been multiplied by a typical surface temperature of 290 K.

mospheric transmittance τ as it has absorbed the effect of the atmospheric path length correction. If the dynamical range of τ within the scenes under consideration is very narrow, then using such an effective emissivity might be justified.

For reference, we have listed the numerical values for Ω_p for several frequencies f and EIA and for selected values of wind speed W and atmospheric transmittance τ in Appendix B.

VI. Wind-Directional Signal: Stokes Parameters

We now turn to the model function ΔE_φ for the four Stokes parameters of the wind direction signal. The general form is a harmonic (Fourier) expansion in the wind direction φ relative to the azimuthal look. From an analysis of reflection symmetric media [37], it follows that the model function for v-pol and h-pol is an even function in φ and the model function for the third and fourth Stokes' parameters S3 and S4 is an odd function in φ. It is found that it is sufficient to keep terms up to second order in the Fourier expansion

$$\Delta E_\varphi^{p,f}(\theta_i;W,\varphi)=\begin{cases} A_1^{p,f}(\theta_i;W)\cdot\cos(\varphi) \\ \quad +A_2^{p,f}(\theta_i;W)\cdot\cos(2\varphi), & p=v,h \\ A_1^{p,f}(\theta_i;W)\cdot\sin(\varphi) \\ \quad +A_2^{p,f}(\theta_i;W)\cdot\sin(2\varphi), & p=S3,S4. \end{cases} \tag{24}$$

Like it was the case for the isotropic emissivity signal ΔE_W, also the wind direction signal ΔE_φ could have a residual dependence on T_S and S. A first guess would be to assume that ΔE_φ is proportional to the specular emissivity $E_0^{p,f}(T_S,S)$ similar as in (17). The smallness of the wind direction signal makes it hard to reliably extract the SST dependence of ΔE_φ from our data, and we therefore do not introduce it at this point.

In order to analyze the dependence of $\Delta E_\varphi^{p,f}(\theta_i;W,\varphi)$ as function of W and φ, we average the values for $\Delta E_\varphi^{p,f}$ simultaneously into discrete wind speed bins of 0.5 m/s size and into discrete wind direction bins of 10°.

Fig. 11 shows the directional signals for the WindSat and SSM/I v-pol and h-pol channels obtained from data sets WS2 and SS of Table I. The sizes of typical error bars range from about ±0.8 K for the 6.8-GHz v-pol to about ±2.0 K for the 37.0-GHz h-pol channels. Within those margins of errors, there is good agreement between the WindSat (set WS2) and SSM/I (set SS) results at 18.7/19.3 GHz and at 37 GHz. The error bars at 85.5 GHz are large: about ±5 K for v-pol and twice as large for h-pol. Still, when averaging over the large data sets, Fig. 11 indicates a wind direction signal at 85.5 GHz for both polarizations, which has about the same shape and size as the 37.0-GHz signals. In our model function, we will assume that the wind direction signal stays constant as function of frequency above 37.0 GHz.

The errors bars at the higher frequencies arise largely because of errors in the atmospheric transmittance τ. As discussed in detail in [10], a small error in the atmospheric parameters causes an error in the isotropic part of the TOA TB, which can easily swamp the small directional signal. For the EIA range in our data sets, the atmospheric error causes the error in the h-pol signal to be about twice as large as in the v-pol signal. This can be seen from the RTM (1) if one makes the simplifying assumption that the atmospheric temperature profile including the surface temperature is a constant value $T(h)\approx T_S\equiv T_{eff}$. The dominant contribution in (1) reduces then to the simple expression $T_{B,p}\approx(1-R_p\tau^2)\cdot T_{eff}$. An error $\Delta\tau$ translates into an error $\Delta T_B\approx -2\tau R_p T_{eff}\cdot\Delta\tau$. If the combination $2\cdot v-h$ is analyzed, the error bars get significantly reduced, because $R_h\approx 2R_v$ for the frequencies and EIA in our data sets.

The results for the harmonic coefficients A_i as function of W are shown in Fig. 12 for $p=v,h$ and in Fig. 13 for $p=S3,S4$. The filled symbols correspond to data set WS1, and

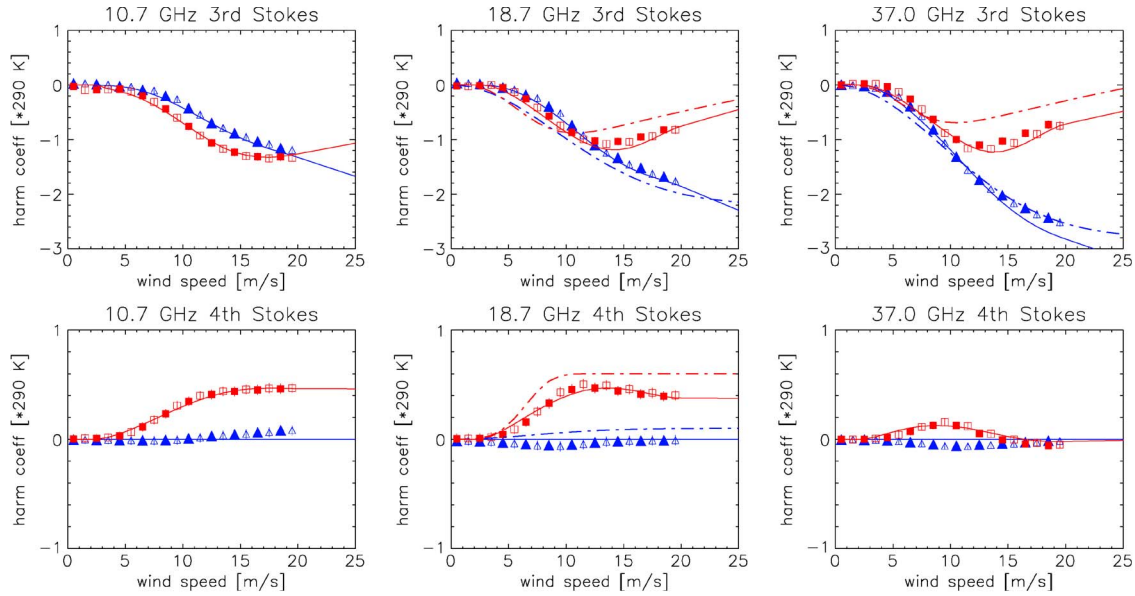

Fig. 13. Same as Fig. 12 but for the third and fourth Stokes parameters.

the open symbols correspond to data set WS2 from Table I. The results from both sets agree within the margins of error. The dash-dot lines in both figures are fits to the measurements of the polarimetric airborne radiometer WINDRAD [38] for the channels where they exist. The dashed lines in Fig. 12 indicate the fit from [10] where existing, which is at 10.7, 18.7, and 37. 0 GHz. The data sets from [10] did not contain a sufficient population above 14 m/s, and therefore the harmonic coefficients had been kept at their values at 14 m/s. For lower wind speeds, our new values agree very well with the results of our older analysis for the dominant harmonic coefficients, which are first harmonic v-pol and second harmonic h-pol. In [10], the coefficients of the nondominant harmonics, which are second harmonic v-pol and first harmonic h-pol were set to zero, because the spread in the data sets that were used in [10] did not allow a more accurate determination. Our new results do indicate a small contribution from those nondominant harmonics, which is also in agreement with [38]. Note that for low—moderate wind speeds, the aircraft flights indicate consistently a slightly stronger directional signal than our WindSat data for all four Stokes parameters. The reason for that could be the very different resolutions at which spaceborne and airborne sensors observe the rough ocean surface. Our results do not give any sizeable value for any of the harmonic coefficients for wind speeds below 3 m/s.

The full lines in Figs. 12 and 13 are polynomial fits for the harmonic coefficients $A_i^{p,f}(W)$. For fitting the curves, we have used a weighted blend of sets WS1 and WS2 from Table I and the data sets from [10] and [12] for wind speeds up to 15 m/s. At higher wind speed, we have also included the results from [13] for S3 and S4 and from [38] for v-pol and h-pol. Because all data sets give close results, choosing the weights amounts more or less to fine tuning the fit in order to obtain reasonably smooth analytical curves. As we have done for the isotropic signal in Section IV-C, we first quote the form of the harmonic coefficients at the reference EIA $\theta_{ref} = 55.2^\circ$ and then model the dependence on EIA.

At $\theta_{ref} = 55.2^\circ$, the harmonic coefficients are fitted by fifth-order polynomials

$$A_i^{p,f} = \sum_{k=1}^{5} \alpha_{i,k}^{p,f} \cdot W^k \quad p = v, h, S3, S4 \quad i = 1, 2. \tag{25}$$

The values for the expansion coefficients $\alpha_{i,k}^{p,f}$ for selected frequencies are listed in Tables III and IV.

The fits apply between 3 and 20 m/s. Above 20 m/s, a linear extrapolation is done. If ever used for wind speeds below 3 m/s, the curves should be smoothly interpolated to 0 from whatever small value they have at 3 m/s, because in some cases, taking the polynomial fit (25) literally would give an unrealistic behavior below 3 m/s. For an arbitrary frequency between 6.8 and 37.0 GHz, the value of the harmonic coefficient can be linearly interpolated from the frequency in the tables. As mentioned earlier, we assume the signal to be constant above 37.0 GHz. To our knowledge, no reliable, published measurements for S3 and S4 exist below 10.7 or above 37.0 GHz, and we do not attempt to provide a function for the harmonic coefficients in these cases.

In order to model the dependence of ΔE_φ on EIA, we need again ingest results from other studies and measurements. It is convenient to work in terms of the true Stokes parameters S1 and S2 rather than v-pol and h-pol itself: $S1 = (v + h)/2$, $S2 = v - h$. At nadir, several constraints exist for the harmonic coefficients due to the symmetry of the looking geometry [39]. Because there is no asymmetry between up and down-wind looks, all of the first harmonic coefficients must vanish: $A_1^{p,f}(\theta_i = 0) \equiv 0$. As there is complete symmetry with respect to the azimuthal look, the transformation properties of the electric field vector dictates that $A_2^{S_1,f}(\theta_i = 0) = A_2^{S_4,f}(\theta_i = 0) \equiv 0$ and $A_2^{S_2,f}(\theta_i = 0) = -A_2^{S_3,f}(\theta_i = 0)$. [40] provides airborne measurements of the wind direction signal at nadir over the frequency range 7–37 GHz. For determining the nadir coefficient $A_2^{S_2,f}(\theta_i = 0)$, we use the spectral behavior $s(f)$

TABLE III
FIRST HARMONIC COEFFICIENTS $\alpha_{1,k}$ FROM (25)

f [GHz]	p	1	2	3	4	5
6.8	v	4.46633E-07	3.34314E-07	3.12587E-06	-1.99336E-07	3.55175E-09
6.8	h	2.17314E-05	-1.54052E-06	7.43743E-07	-3.32899E-08	3.04367E-10
10.7	v	4.96132E-05	-2.90991E-05	9.05913E-06	-5.73703E-07	1.10332E-08
10.7	h	-2.20699E-05	8.92180E-06	4.69873E-08	-2.41047E-08	5.71120E-10
10.7	S3	-8.48737E-05	5.35295E-05	-1.16605E-05	6.83923E-07	-1.27622E-08
10.7	S4	0.00000E+00	0.00000E+00	0.00000E+00	0.00000E+00	0.00000E+00
18.7	v	-4.88686E-05	-2.26779E-06	9.94735E-06	-7.51560E-07	1.55400E-08
18.7	h	3.95872E-05	-2.88339E-05	6.61597E-06	-4.08181E-07	7.87906E-09
18.7	S3	-3.29350E-05	4.32977E-05	-1.33822E-05	8.75024E-07	-1.74093E-08
18.7	S4	0.00000E+00	0.00000E+00	0.00000E+00	0.00000E+00	0.00000E+00
37.0	v	-2.41163E-04	7.66737E-05	3.65641E-06	-5.59326E-07	1.35655E-08
37.0	h	-5.43465E-05	2.24360E-05	1.16736E-06	-1.58769E-07	3.60149E-09
37.0	S3	2.55925E-04	-1.02271E-04	3.06653E-06	6.84854E-08	-2.83830E-09
37.0	S4	0.00000E+00	0.00000E+00	0.00000E+00	0.00000E+00	0.00000E+00

TABLE IV
SECOND HARMONIC COEFFICIENTS $\alpha_{2,k}$ FROM (25)

f [GHz]	p	1	2	3	4	5
6.8	v	2.21863E-04	-1.18053E-04	1.68718E-05	-8.94076E-07	1.60273E-08
6.8	h	-3.50262E-06	1.02052E-05	-5.28636E-06	3.82864E-07	-7.87283E-09
10.7	v	1.48213E-04	-7.15954E-05	1.01992E-05	-5.41575E-07	9.71451E-09
10.7	h	-8.09058E-05	6.06930E-05	-1.42500E-05	8.86313E-07	-1.69340E-08
10.7	S3	-1.90531E-04	1.09714E-04	-1.97712E-05	1.10888E-06	-1.96980E-08
10.7	S4	-9.49332E-05	3.91201E-05	-1.64418E-06	-2.12315E-08	1.47529E-09
18.7	v	1.21860E-04	-6.39714E-05	9.34100E-06	-5.24394E-07	9.97506E-09
18.7	h	2.65036E-04	-9.32568E-05	1.41605E-06	2.98507E-07	-9.64763E-09
18.7	S3	1.66139E-04	-4.39714E-05	-5.42274E-06	6.82097E-07	-1.69151E-08
18.7	S4	-1.62337E-04	7.13779E-05	-5.42054E-06	1.26564E-07	-3.00476E-10
37.0	v	2.35250E-04	-1.24502E-04	1.48805E-05	-7.07241E-07	1.18776E-08
37.0	h	7.26916E-04	-2.84727E-04	2.20935E-05	-5.68143E-07	3.00983E-09
37.0	S3	1.37851E-04	-1.58017E-05	-9.08052E-06	9.03144E-07	-2.16700E-08
37.0	S4	-1.33456E-04	7.09317E-05	-8.67173E-06	3.98910E-07	-6.31997E-09

from the results of [40], which is very similar than the spectral behavior for our results at high EIA

$$A_2^{S_2,f}(\theta_i = 0, W) = u(W) \cdot s(f)$$
$$u(W) = [W^2 - W^3/22.5]/55.5556,$$
$$s(f) = \frac{2}{290} \cdot \left[1.0 - \log_{10}\left(\frac{30.0}{f}\right)\right] \quad (26)$$

where f is measured in GHz. $s(f)$ is kept constant above 37.0 GHz. The form of the wind speed dependence $u(W)$ was chosen so that it mimics our results for both v-pol and h-pol at the high EIA and $u(10\ \text{m/s}) = 1$, which renders the results of [40] at 10 m/s. $u(W)$ is kept constant above 15 m/s. For the EIA dependence of $A_i^{S_2,f}$, we use the same form as for the isotropic signal (16)

$$A_i^{s,f}(\theta_i, W, \ldots) = A_i^{s,f}(\theta_i = 0, W, \ldots) + \left[A_i^{s,f}(\theta_{ref}, W, \ldots) - A_i^{s,f}(\theta_i = 0, W, \ldots)\right] \cdot \left(\frac{\theta_i}{\theta_{ref}}\right)^{x_{si}}$$
$$s = S1, S2, S3, S4 \quad i = 1, 2 \quad (27)$$

if $\theta_i \geq \theta_{ref}$ and linearly extrapolate above θ_{ref}. We chose the exponents x_{si} so that the θ_i dependence is consistent with the aircraft measurements of [38], which were performed at EIA 45°, 55°, and 65°. The values of x_{si} are listed in Table V, and they are the same values for all frequencies.

TABLE V
VALUES OF THE EXPONENT x_{si} IN THE EIA DEPENDENCE OF ΔE_φ (27)

i	s	S1	S2	S3	S4
1		2.0	1.0	1.0	2.0
2		2.0	4.0	4.0	2.0

Finally, we want to note that we have not introduced an atmospheric path length correction for the wind direction signal, or, in other words, we have assumed that the atmospheric path length correction $T_{B,scat}$ from Section V is independent on the relative wind direction φ. As a consequence, $T_{B,scat}$ does not contribute to S3 or S4. If $T_{B,scat}$ depends on φ, then this contribution can be absorbed into an effective wind direction signal $\Delta E_\varphi^*(W, \varphi, \tau)$ similar like it was done in (23) of Section V for the isotropic signal. This effective wind direction signal will then depend on the atmospheric transmittance τ. In order to check this, we have calculated a set of $\Delta E_{\varphi,\tau}$ for a set of τ-intervals that span the whole dynamical range of τ within our data. We have confirmed that $\Delta E_{\varphi,\tau}$ is essentially the same in each τ-interval for each channel within the margins of error. That means that within our framework, it is justified to drop the τ-dependence in $\Delta E_\varphi^*(W, \varphi, \tau)$ and work with a τ-independent $\Delta E_\varphi(W, \varphi)$ that way also dropping any φ-dependence in $T_{B,scat}$. As a consequence, the parameterization (21) takes a simple form for the polarimetric WindSat channels $p = +45°, -45°, lc, rc$. Because of energy conservation

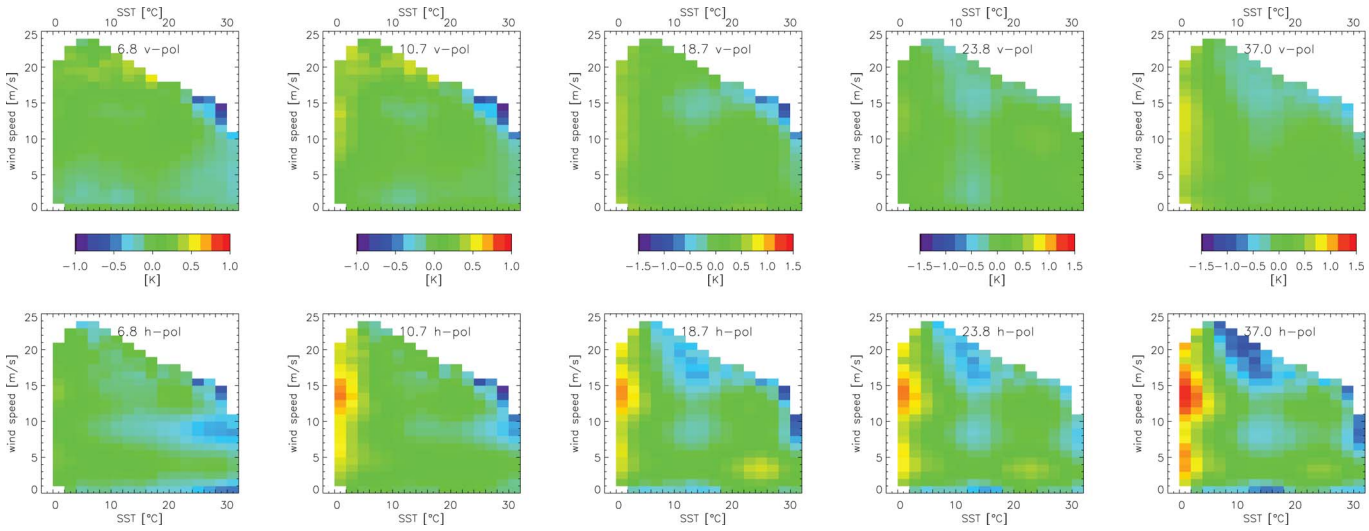

Fig. 14. Measured minus computed TB for WindSat v-pol and h-pol channels as function of SST and wind speed. The computation uses the RTM with the emissivity model function presented in this paper. The wind speeds are from QuikSCAT (set WS2 from Table I).

$T_{B,v} + T_{B,h} = T_{B,+45^\circ} + T_{B,-45^\circ} = T_{B,lc} + T_{B,rc}$ and also $E_v + E_h = E_{+45^\circ} + E_{-45^\circ} = T_{lc} + T_{rc}$, which imply that

$$\Omega_{+45^\circ} = \Omega_{-45^\circ} = \Omega_{lc} = \Omega_{rc} = \frac{R_v \cdot \Omega_v + R_h \cdot \Omega_h}{R_v + R_h}. \quad (28)$$

VII. Validation and Error Assessment

We now try to assess the accuracy of our emissivity model function. There are two basic methods to do that. The first one is to analyze the difference between measured and RTM computed TOA TB as function of independent measured "ground truth" parameters, SST and wind speed being the most important ones. The second and simpler way is a direct comparison of the geophysical parameters that were derived by a physical algorithm, which is based on this emissivity model. Though a full validation of the geophysical parameters will be the subject of a separate publication, we want to highlight some of the most important results here.

Both methods have their limitations, which needs to be kept in mind when trying to assess the accuracy of the RTM. An important issue for both methods is the quality of the "ground truth" data themselves. For example, there could be a systematic error in the Reynolds SST or the QuikSCAT wind speeds from data set WS2. Because the retrieval algorithm for the environmental parameters uses several channels simultaneously, checking the environmental parameters does not allow to pin down problems with the model function of a specific channel, but merely provides an overall assessment of the model functions of those channels that are most sensitive to the parameter under consideration. Finally, an error in the atmospheric absorption model or any residual systematic error in water vapor and cloud water that is correlated with the surface parameters will show up in the measured minus computed TB.

Fig. 14 displays the averages of measured minus computed TOA TB of the WindSat channels in data set WS2 as 2-D function of Reynolds SST and QuikSCAT wind speed. For making an assessment of the quality of the emissivity model, it is important to know the population of this 2-D SST—wind speed array, which is shown in Fig. 15. SST—wind speed bins that have a population of less than 0.1% of the maximum population are not displayed in Fig. 14. Fig. 16 contains the results for measured minus computed TB for the 85.5-GHz channels of data set SS. Note the different color scales for the different frequencies.

We are analyzing the average TB differences but not the standard deviations. The latter one is largely dominated by random errors in the atmospheric parameters (water vapor and cloud water) and by sampling mismatch errors between the satellite measurements and the "ground truth" data. This includes also random errors in the ground truth data themselves. Other, smaller contributions to the standard deviation errors are the radiometer noise figures. The standard deviation error would also contain errors that might arise if the ocean surface roughness was influenced by additional parameters, such as wave height or development of the sea state, which have not been part of our emissivity model. In order to determine the accuracy of the emissivity model, we assess in sufficiently dense populated areas of the SST—wind speed array how much the measured minus computed TOA TB deviate from their ideal value, which is zero. Figs. 14 and 16 both probe simultaneously the accuracy of the specular emissivity, which is determined by the dielectric constant of sea water, and the accuracy of the wind-induced emissivity model.

Aside from marginal, very sparsely populated regions of the SST—wind speed array, Figs. 14 and 16 show an excellent match between measured and RTM computed TB for all wind speed and SST bins. The most noticeable exception is the h-pol emissivity at low temperatures. The figures indicate that the model function underestimates the true emissivity at low SST particularly if the wind speeds are either low or high. The problem increases with frequencies being absent at 6.8 GHz, very weak at 10.7 GHz and reaching about 3 K in the TOA TB at 85.5 GHz. Because the v-pol channels seem much less or not at all affected, this is unlikely indicating a significant problem with the dielectric constant model, as an error in the specular

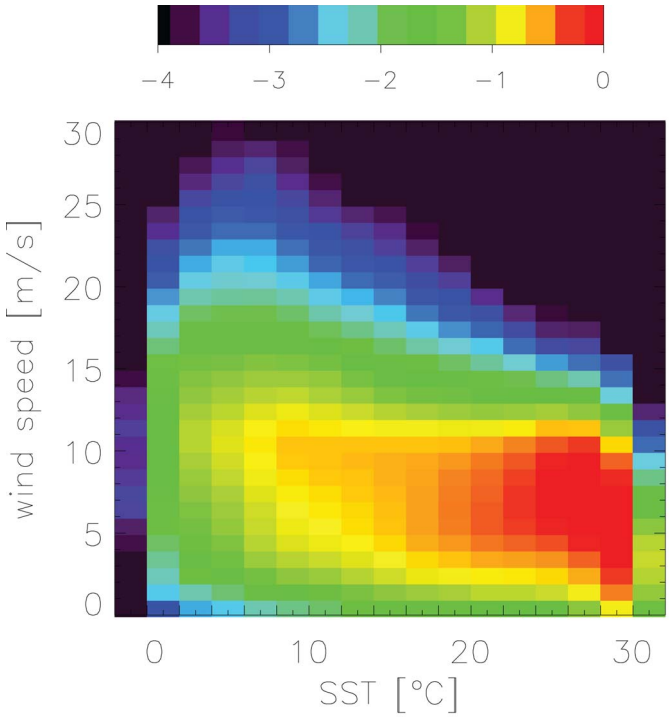

Fig. 15. Population density of the SST—wind speed array in Fig. 14 relative to its maximum value. The figure displays $\log_{10}[N(T_S, W)/N_{\max}]$, where $N(T_S, W)$ is the number of events within the bin that is centered on surface temperature T_S and wind speed W and $N_{\max}$ is the maximum of all bins.

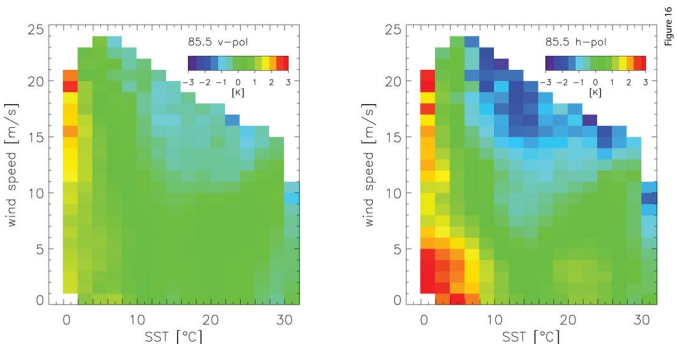

Fig. 16. Measured minus computed TB as function of SST and wind speed for the 85.5-GHz v-pol (left panel) and 85.5-GHz h-pol (right panel). The wind speeds are from QuikSCAT (set SS from Table I).

emissivity would show stronger in the v-pol than in the h-pol TB [26]. That leaves one or a combination of the following scenarios as probable cause.

1) The value of the water vapor or liquid cloud water that is retrieved by the radiometer is too high in those regions.
2) The water vapor continuum absorption that is used in the RTM function is too high in those regions.
3) The assumption (15) that the temperature dependence of the wind-induced emissivity ΔE_W is proportional to the specular emissivity E_0 breaks down at low SST for the h-pol channels at higher frequencies.
4) The observed deficiency at higher wind speeds could be caused by an inaccuracy in the in the atmospheric path length correction Ω_p for the scattered downwelling atmospheric radiation, which we have calculated using the GO model (cf. Section V).
5) The assumption (13) that ΔE_W goes to zero with wind speed is not valid anymore in those cases, but ΔE_W stays finite and the ocean would maintain some residual roughness even at low winds. This possibility has been mentioned in other studies [33]. Our results show that, if true, it would apply in regions with cold SST, and the sensitivity to this residual roughness would increase with the frequency of the radiation.

Both figures indicate small positive and negative differences of the RTM computed TB versus the measurements compared to the ideal case. The most noticeable one is observed in the 6.8-GHz h-pol at around 10 m/s wind speed, which reaches about 0.5 K in size. Those oscillations are most likely due to the fact that the fifth-order polynomial fit (18) might not fully reflect the real behavior of the wind-induced emissivity in those cases.

The environmental parameter that is most sensitive to the ocean emissivity model is SST. The dominant contributions come from the low frequency channels (6.8 and 10.7 GHz) and among those, the v-pols have the strongest SST dependence. The sizes of an error in SST and an error in the v-pol 6.8-GHz TB scale roughly like 2:1 [1]. Fig. 17 shows the difference between WindSat and the Reynolds OI SST binned as function of Reynolds SST (left panel) and WindSat wind speed (right panel). A small oscillation in the SST difference as function of wind speed and the upward trend of about 1.0 K between 15 m/s and 20 m/s wind speeds is visible in the right panel. It points most likely to a deficiency of the wind-induced emissivity model at these wind speeds in the order of 0.5 K or less. A very small upward trend of about 0.2 K in the SST difference is observed between 0 and 15 m/s wind speed. Over the whole dynamical SST range, we find a roll-off in the SST difference of only about 0.3 K at both the high and the low SST end compared with its value at 20 °C. In the retrieval of the geophysical product, those small crosstalk biases can be eliminated by deriving a static post-hoc correction table, which consists of the bias values and which is then subtracted from the geophysical parameter in the last step of the retrieval algorithm.

In summary, our analysis suggests that in the EIA range between 49°–56°, which is covered by the WindSat and SSM/I sensors, the accuracy of our model for the ocean surface emissivity containing both the specular as well as the wind-induced emissivity is roughly about ±0.2 K at the 6.8-GHz v-pol, increases to about ±0.5 K at the 37.0-GHz h-pol, and reaches pm1.5 K at the 85.5-GHz h-pol. Those values apply as long as cases with very sparse occurrence are excluded.

VIII. Emissivity at High Wind Speeds

The analysis performed so far is valid up to wind speeds of about 18 m/s. Due to sparseness of reliable measurements, the determination of the wind-induced emissivity at high wind speeds becomes more difficult. Its knowledge is of course crucial for the radiometer measurement of wind speeds in storms. In [13], both ΔE_W and ΔE_φ for S3 and S4 were determined from collocations of WindSat TB and hurricane wind fields from the HRD analysis, which comprises our data set WS3 from Table I. Because most tropical cyclone winds are

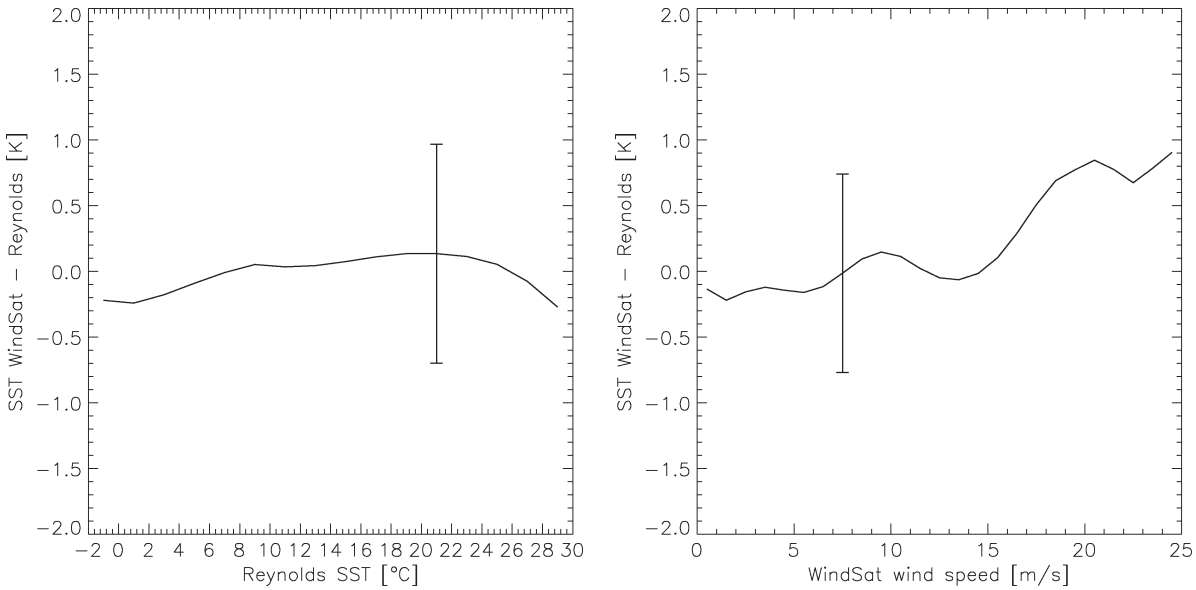

Fig. 17. Difference between SST from WindSat and Reynolds OI [22] as function of SST (left panel) and wind speed (right panel) with typical error bars.

contaminated by rain, the big challenge is to accurately remove the effect of rain in the atmospheric τ, T_{BU}, T_{BD} when solving the RTM equation for the emissivity as shown in Section II-C. This causes the random error bars for data set WS3 being significantly larger than for the other cases. The details on how to remove this atmospheric rain effect has been described in [13]. We will now check if and how well the results of [13] match the ones of our current study in the transition region, say between 18 and 20 m/s. This is exhibited in the left panel of Fig. 3, the circles being the results from set WS3. The dashed lines are a linear fits to those data for wind speeds above 20 m/s. It is evident for both polarizations that the slopes of the dashed lines match very well with the slopes of linear fits to data sets WS1 (red squares) and WS2 (blue diamonds) between 18 and 20 m/s. Though not explicitly shown, we find that this applies also to the higher frequency channels, even though the error due to rain in the atmosphere increases strongly with frequency. That itself is a very satisfying result, as the analyses of data sets WS1/WS2 and data set WS3 are completely independent of each other.

Fig. 3 shows a constant offset between set WS2 and the two other sets. This offset could be caused by either or both a systematic error in handling the atmospheric parameters in set WS3 or a systematic error in some of the HRD wind speeds. It should also be noted that various assumptions had been made in [13] when trying to match the spatial and temporal scale of the HRD wind fields to those of the WindSat TB. It is possible that this systematic offset is caused by those assumptions rather than the HRD analysis itself. When fitting the final curves, which are the full black lines in Fig. 3, we have constrained the fifth-order polynomials from (18) to so that their slopes are the same as those obtained from data set WS3 at $W_0 = 20$ m/s. Our analysis clearly suggest that ΔE_W is linearly increasing with wind speed above W_0.

We will now perform some additional independent checks of our high wind speed emissivity model function. The results of five field campaigns measuring wind vectors by an aircraft turbulent probe during early 2007 and a comparison with scatterometer and NWP winds over the Denmark strait and Irminger Sea near Greenland were reported in [41]. The dynamical wind speed range of these measurements covers the interval between 5 and 28 m/s. We have repeated their analysis using WindSat wind speeds that were derived with our new emissivity model. Fig. 18 shows the results. The right panel uses the 21-km WindSat wind speeds using all channels above and including 18.7 GHz. The left panel uses the 35-km resolution WindSat wind speed that uses all channels above and including 10.7 GHz. The 10.7-GHz channel allows an accurate wind speed retrieval in rain using the global wind speed through rain algorithm from [13], which is not possible with only the higher frequencies. The first field campaign B268 of [41] (purple triangles in the left panel of Fig. 18) did contain light rain, and therefore only a 35-km resolution retrieval was performed. Fig. 18 also contains values for total bias, standard deviation, linear slope, and Pearson correlation between the WindSat and the aircraft wind speed measurements. We observe an excellent correlation between aircraft and WindSat data set, which is much better than for any of the other data sets that had been studied in [41]. The 35-km resolution WindSat wind speeds seem to be systematically high by about 1.6 m/s. For the 21-km resolution winds, this offset is only about 0.9 m/s. Because all the flights are very close to land and the sea ice edge, the most likely scenario is that either land or sea ice or both of them enter the WindSat field of view, possibly through the sidelobes. This affects the 10.7 GHz significantly more than the higher frequencies, because the 10.7-GHz footprint size is larger and also because the radiometerically cold 10.7-GHz h-pol ocean TB is more sensitive to any contamination from radiometerically warm land or sea ice.

Another good candidate for an independent cross check of our high wind emissivity model is the C-band emissivity model function that was developed from SFMR flights at nadir [15] and recently extended to higher EIA by the CFRSL group [16]. Wind speeds from dropsondes that were extrapolated to

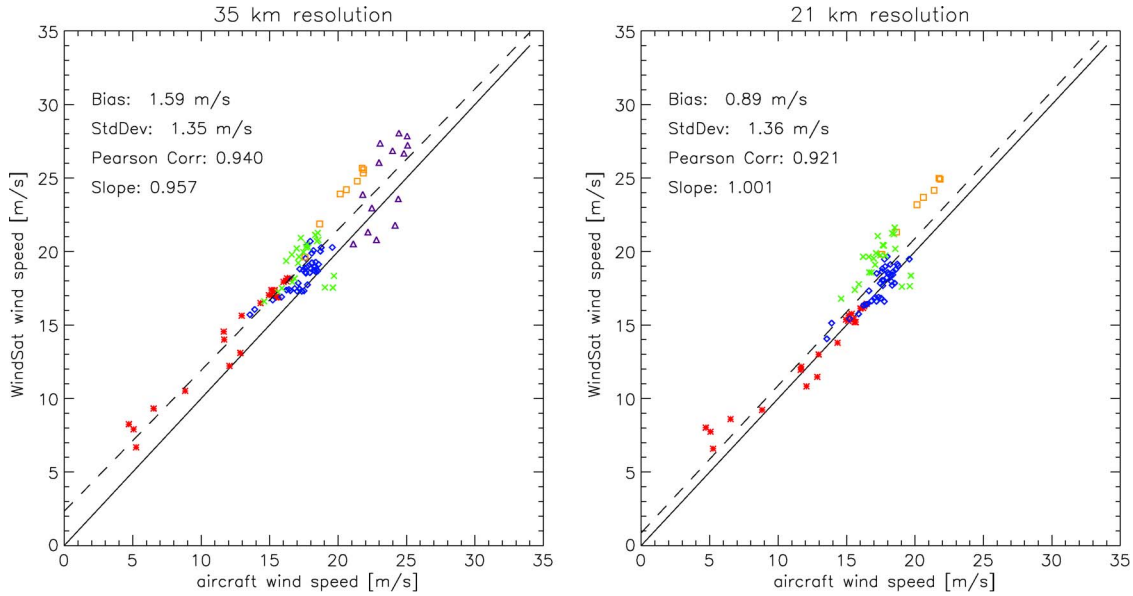

Fig. 18. Comparison of wind speeds from WindSat with the measurements from [41] over the Denmark Strait and Irminger Sea using an aircraft turbulent probe. Left panel: using 10.65 GHz and higher frequencies (35-km resolution) + wind speed retrievals through rain algorithm [13], right panel: using 18. 7 GHz and higher frequencies (21-km resolution) + rain-free wind speed algorithm. The symbols indicate data taken from the five different missions of [41]: B 268 (purple triangles), B 271 (red stars), B 276 (blue diamonds), B 277 (orange squares), B 278 (green crosses). The dashed line indicate the linear fit of the data. The full lines indicate the ideal cases. The figures also list the values for bias, standard deviation, Pearson correlation coefficient, and the slope of the linear fit of WindSat versus aircraft wind speeds.

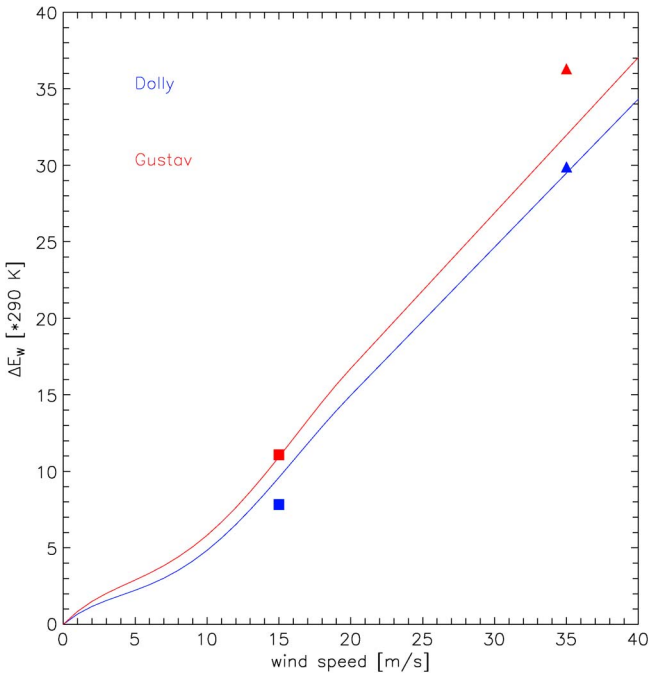

Fig. 19. C-band h-pol wind-induced (excess) ocean emissivities measured by the NOAA HRD airborne SFMR during hurricanes Gustav at EIA: 45° (red) and Dolly at EIA 30° (blue) [16]. The measurements were taken in rain-free regions at wind speeds of 15 m/s (squares) and 35 m/s (triangles). The full lines are the model functions from Section IV of this paper. The emissivities were shifted to a common frequency of 6.8 GHz and multiplied by a typical surface temperature of 290 K.

the sea surface were used as ground truth data for developing the SFMR/CFRSL model functions. In order to compare with our C-band model function at 6.8 GHz, we have adjusted the SFMR/CFRSL results, which are referenced to 5.3 GHz, based on the frequency behavior reported in [34].

Let us first consider the h-pol SFMR emissivity measurements that were taken during hurricanes Gustav and Dolly during 2008 in rain-free scenes at 30° and 45° EIA and at 15 m/s and 35 m/s wind speeds. The results were reported in [16]. Because the scenes were not contaminated by rain, those data provide a good test of our emissivity model function as there are no possible systematic errors due to removing the rain effect in the TB measurements. Fig. 19 shows the Gustav and Dolly data together with our model function. We observe excellent agreement. The only exception of the hurricane Gustav measurement that was taken at 40° and 35 m/s. In that case, our emissivity model comes in too low by about 3 K, which nevertheless still lies within the margins of error.

Finally, Fig. 20 compares the wind-induced emissivity model functions from SFMR/SCRSL and our study at nadir. The most important difference is that SFMR model function rises quadratically between 7.0 m/s and 31.9 m/s and linearly above 31.9 m/s. As we just have discussed, all of our data sets clearly indicate that the emissivity increases linearly with wind speed already at around 20 m/s and keeps doing that also at higher winds. It should be noted that the SFMR/CFRSL model does not contain the atmospheric path length correction that was discussed in Section V. This has an effect even at C-band frequencies, as some of the measurements that went into [15] and [16] are likely heavily contaminated by rain, particularly at high wind speeds. We should therefore compare the SFMR/CFRSL model function with the he effective emissivity ΔE_W^* from (23). This is the dashed black line in Fig. 20 where we have assumed a typical correlation between wind speed and atmospheric transmittance for hurricane atmospheres [13]. That brings the SFMR/CFRSL and our nadir model functions closer together. As a matter of fact, within the margins of errors, both model functions are consistent up to about 30 m/s. We currently

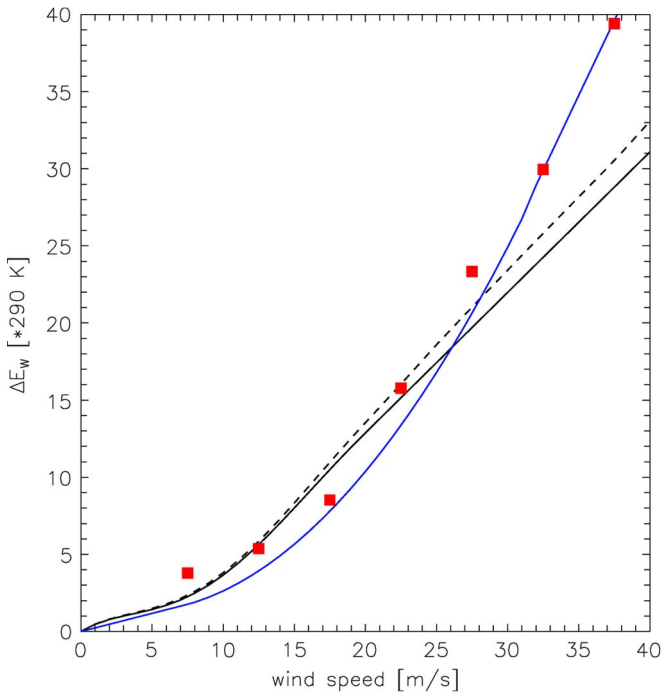

Fig. 20. Comparison of C-band nadir wind-induced (excess) ocean emissivities: SFMR measurements [15] (blue curve), the CFRSL model function [16] (red squares) and the model function from Section IV of this paper (solid black curve). The dashed black line is the effective emissivity ΔE_W^* from (23) for typical hurricane atmospheres if the atmospheric path length correction is omitted. The emissivities were shifted to a common frequency of 6.8 GHz and multiplied by a typical surface temperature of 290 K.

do not know what causes the discrepancy at higher wind speeds. The following scenarios or a combination of them are possible.

1) The SFMR probes the ocean at a much higher resolution than the satellite sensor does. It is possible that at high wind speeds, the roughness and emissivity responses to wind speed are different at both resolutions.
2) Our derivation of the EIA dependence of ΔE_W in Section IV-C was based mainly on observations at low and moderate wind speeds. It could be that the behavior in (16) does not apply at very low EIA and very high wind speeds. Both the nadir value and also the exponent x_s in (16) could change as a function of wind speed and also frequency. That might lead to the fact that at very low EIA, the emissivity is closer to the 55° h-pol value rather than the arithmetic average between v-pol and h-pol values. That would make its value larger than depicted in our model function.
3) There could be a systematic error in removing the rain contamination from the SFMR/CFRSL measurements, which is correlated with wind speed.

Let us finally point out an important common feature that is evident in both our and the SFMR/CFRSL C-band emissivity model functions. None of them shows any signs of saturation at high wind speeds, which guarantees good sensitivity of the TOA TB to wind speed even at high winds. In view of the recent progress in dealing with the rain effect in the measurement of radiometer wind speeds through rain [13], this suggests that the passive radiometer is well suited for the measuring wind speeds under storm conditions.

TABLE VI
PARAMETERS b_i, $i = 0, 1, 2$ FROM (29)

i	0	1	2
b_i	- 3.33330E-03	4.74868E-06	0

IX. SUMMARY AND CONCLUSION

To summarize: We have determined a model function for the isotropic and wind direction-dependent parts of the wind-induced ocean surface emissivity from WindSat and SSM/I TB observations, which is applicable for wind speeds up to 40 m/s. After combining our results with other established studies, we have extended the validity of our model function to EIA ranging from nadir to 65°. This model function will be a useful tool in current and future airborne and spaceborne measurements of ocean surface parameters such as SST, wind speed, and wind direction. It can also help in the determination of atmospheric quantities such as water vapor or cloud water, because the surface emissivity itself enters in as an uncertainty in the RTM of the channels that measure these parameters. We have demonstrated the accuracy of our model function for 49°–56° EIA by analyzing the match of measured and RTM computed TB and checking the accuracy of SST that is retrieved using this emissivity model. In addition we have also provided numerous cross checks with independent data, which have not been used in the development of the model function such as measurements from TOPEX/Poseidon, aircraft turbulent probes and airborne microwave sensors. Special attention has been given to the high wind speed measurements that were taken by the SFMR. These comparisons have shown that considerable uncertainties only remain in the cases of the higher frequency h-pol channels at cold SST and very high wind speeds above 30 m/s at low EIA.

Our newly developed emissivity model is used as basis of all the physical retrieval algorithms in Remote Sensing System's Version 7 ocean product suite, which is currently being released (http://www.remss.com). The whole data set consists of roughly 100 year worth of spaceborne radiometer measurements of SST, wind speed, water vapor, liquid cloud water, and rain rate from all of the SSM/I, SSMIS, TMI, AMSR-E, AMSR-J, and WindSat. Future missions will be added as soon as they become available. The same RTM is used consistently in all products, which is an essential step in the development of an accurate long-term climate data record.

The final missing stone is the development of a model for the ocean surface emissivity at low frequencies, particularly at L-band. Its knowledge will be crucial for accurate measurements of ocean surface salinity from the Soil Moisture and Ocean Salinity Mission and the AQUARIUS radiometer. As soon as reliable and well-calibrated TOA TB measurements from those instruments become available, we will be able to extend our emissivity model down to L-band frequencies.

APPENDIX A
DIELECTRIC CONSTANT OF SEA WATER

This appendix briefly summarizes the small adjustments of the Debye parameters of the dielectric constant ε of sea water

TABLE VII
PARAMETERS d_i, $i = 0, 1, 2, 3, 4$ FROM (30)

i	0	1	2	3	4
d_i	0.23232E-02	- 0.79208E-04	0.36764E-05	0.35594E-06	0.89795E-08

TABLE VIII
VALUES OF Ω FROM FOR VARIOUS VALUES OF WIND SPEED W AND TRANSMITTANCE τ AT AN EIA OF 65°. THE COMPUTATION USED $T_S = T_{ref}$ AND A TYPICAL ATMOSPHERIC TEMPERATURE OF $T_D = 281$ K

f [GHz]	p	τ	0.95				0.90				0.80				0.70				0.60				0.40				0.20			
		W [m/s]	4	7	12	20	4	7	12	20	4	7	12	20	4	7	12	20	4	7	12	20	4	7	12	20	4	7	12	20
6.8	v		0.02	0.01	-0.02	-0.08	0.01	0.00	-0.03	-0.09	0.00	-0.01	-0.05	-0.11	-0.01	-0.02	-0.06	-0.12	-0.01	-0.03	-0.07	-0.12	-0.03	-0.05	-0.08	-0.13	-0.03	-0.05	-0.08	-0.11
	h		0.12	0.17	0.16	0.10	0.11	0.15	0.14	0.08	0.09	0.11	0.10	0.04	0.07	0.08	0.06	0.01	0.05	0.06	0.03	-0.02	0.02	0.01	-0.01	-0.05	0.00	-0.01	-0.03	-0.06
10.7	v		0.02	0.00	-0.04	-0.11	0.01	-0.01	-0.05	-0.11	0.00	-0.02	-0.07	-0.13	-0.01	-0.04	-0.08	-0.14	-0.02	-0.05	-0.09	-0.14	-0.03	-0.06	-0.10	-0.14	-0.04	-0.06	-0.09	-0.12
	h		0.14	0.18	0.15	0.07	0.12	0.15	0.13	0.05	0.10	0.11	0.08	0.01	0.07	0.08	0.05	-0.02	0.05	0.05	0.02	-0.04	0.02	0.01	-0.02	-0.07	-0.01	-0.02	-0.04	-0.07
18.7	v		0.01	-0.01	-0.07	-0.13	0.00	-0.02	-0.08	-0.14	-0.01	-0.04	-0.09	-0.15	-0.02	-0.05	-0.10	-0.16	-0.03	-0.06	-0.11	-0.16	-0.04	-0.07	-0.12	-0.16	-0.04	-0.07	-0.10	-0.14
	h		0.16	0.18	0.13	0.04	0.14	0.15	0.11	0.02	0.11	0.11	0.07	-0.01	0.08	0.08	0.03	-0.04	0.06	0.05	0.01	-0.06	0.02	0.00	-0.03	-0.08	-0.01	-0.02	-0.05	-0.09
23.8	v		0.01	-0.02	-0.08	-0.15	0.00	-0.03	-0.09	-0.15	-0.01	-0.05	-0.10	-0.16	-0.02	-0.06	-0.11	-0.17	-0.03	-0.07	-0.12	-0.17	-0.05	-0.08	-0.12	-0.17	-0.05	-0.07	-0.11	-0.14
	h		0.16	0.18	0.12	0.03	0.15	0.15	0.10	0.01	0.11	0.11	0.06	-0.02	0.08	0.08	0.03	-0.05	0.06	0.05	0.00	-0.07	0.02	0.00	-0.04	-0.09	-0.01	-0.03	-0.05	-0.09
37.0	v		0.00	-0.04	-0.10	-0.16	-0.01	-0.05	-0.11	-0.17	-0.02	-0.06	-0.12	-0.18	-0.03	-0.08	-0.13	-0.19	-0.04	-0.08	-0.14	-0.19	-0.05	-0.09	-0.14	-0.18	-0.05	-0.08	-0.12	-0.15
	h		0.18	0.18	0.11	0.02	0.16	0.15	0.09	0.00	0.12	0.11	0.05	-0.04	0.09	0.07	0.02	-0.06	0.06	0.04	-0.01	-0.08	0.02	0.00	-0.04	-0.10	-0.01	-0.03	-0.06	-0.10
89.0	v		-0.01	-0.06	-0.12	-0.19	-0.02	-0.07	-0.13	-0.19	-0.04	-0.09	-0.15	-0.20	-0.05	-0.10	-0.16	-0.21	-0.06	-0.11	-0.16	-0.21	-0.07	-0.11	-0.16	-0.20	-0.07	-0.10	-0.14	-0.17
	h		0.20	0.18	0.10	0.00	0.17	0.15	0.08	-0.02	0.13	0.11	0.03	-0.05	0.10	0.07	0.00	-0.08	0.07	0.04	-0.02	-0.09	0.02	-0.01	-0.06	-0.11	-0.01	-0.03	-0.07	-0.11

TABLE IX
SAME AS TABLE VIII, BUT AT AN EIA OF 55°

f [GHz]	p	τ	0.95				0.90				0.80				0.70				0.60				0.40				0.20			
		W [m/s]	4	7	12	20	4	7	12	20	4	7	12	20	4	7	12	20	4	7	12	20	4	7	12	20	4	7	12	20
6.8	v		0.03	0.06	0.09	0.10	0.03	0.05	0.08	0.08	0.02	0.04	0.06	0.05	0.02	0.03	0.04	0.03	0.01	0.02	0.02	0.01	0.00	0.00	0.00	-0.02	-0.01	-0.01	-0.02	-0.03
	h		0.06	0.13	0.21	0.24	0.06	0.12	0.18	0.21	0.05	0.10	0.14	0.16	0.04	0.08	0.11	0.12	0.04	0.06	0.08	0.09	0.02	0.03	0.04	0.03	0.00	0.01	0.00	0.00
10.7	v		0.04	0.07	0.09	0.09	0.03	0.06	0.08	0.07	0.03	0.05	0.05	0.04	0.02	0.03	0.03	0.02	0.01	0.02	0.02	0.00	0.00	0.00	-0.01	-0.02	-0.01	-0.01	-0.02	-0.04
	h		0.08	0.15	0.22	0.24	0.07	0.14	0.20	0.21	0.06	0.11	0.15	0.15	0.05	0.09	0.12	0.11	0.04	0.07	0.09	0.08	0.02	0.03	0.04	0.03	0.01	0.01	0.00	-0.01
18.7	v		0.04	0.07	0.09	0.08	0.04	0.06	0.07	0.06	0.03	0.05	0.05	0.03	0.02	0.03	0.03	0.01	0.01	0.02	0.01	-0.01	0.00	0.00	-0.02	-0.03	-0.01	-0.02	-0.03	-0.04
	h		0.10	0.18	0.24	0.23	0.09	0.16	0.21	0.20	0.08	0.13	0.16	0.15	0.06	0.10	0.12	0.11	0.05	0.08	0.09	0.07	0.03	0.04	0.04	0.02	0.01	0.01	0.00	-0.01
23.8	v		0.04	0.07	0.09	0.07	0.04	0.06	0.07	0.05	0.03	0.05	0.04	0.03	0.02	0.03	0.02	0.00	0.01	0.02	0.01	-0.01	0.00	-0.01	-0.02	-0.04	-0.01	-0.02	-0.03	-0.05
	h		0.11	0.19	0.24	0.23	0.10	0.17	0.21	0.20	0.08	0.14	0.16	0.14	0.07	0.11	0.12	0.10	0.05	0.08	0.09	0.07	0.03	0.04	0.04	0.02	0.01	0.01	0.00	-0.01
37.0	v		0.04	0.07	0.08	0.06	0.04	0.06	0.06	0.04	0.03	0.04	0.03	0.01	0.02	0.02	0.01	-0.01	0.01	0.01	0.00	-0.03	0.00	-0.01	-0.03	-0.05	-0.01	-0.02	-0.04	-0.05
	h		0.13	0.21	0.25	0.23	0.11	0.19	0.22	0.19	0.10	0.15	0.17	0.14	0.08	0.12	0.13	0.10	0.06	0.09	0.09	0.07	0.03	0.04	0.04	0.02	0.01	0.01	0.00	-0.02
89.0	v		0.04	0.05	0.05	0.03	0.03	0.04	0.03	0.01	0.02	0.02	0.01	-0.01	0.01	0.01	-0.01	-0.03	0.00	-0.01	-0.02	-0.05	-0.01	-0.02	-0.04	-0.06	-0.02	-0.03	-0.05	-0.06
	h		0.16	0.25	0.27	0.23	0.15	0.22	0.24	0.19	0.12	0.17	0.18	0.14	0.10	0.13	0.13	0.10	0.08	0.10	0.10	0.06	0.04	0.05	0.04	0.01	0.01	0.01	0.00	-0.02

TABLE X
SAME AS TABLE VIII, BUT AT AN EIA OF 45°

f [GHz]	p	τ	0.95				0.90				0.80				0.70				0.60				0.40				0.20			
		W [m/s]	4	7	12	20	4	7	12	20	4	7	12	20	4	7	12	20	4	7	12	20	4	7	12	20	4	7	12	20
6.8	v		0.03	0.05	0.10	0.16	0.03	0.05	0.10	0.15	0.02	0.04	0.08	0.12	0.02	0.04	0.07	0.09	0.02	0.03	0.05	0.07	0.01	0.02	0.03	0.04	0.00	0.01	0.01	0.01
	h		0.04	0.08	0.16	0.26	0.04	0.08	0.15	0.23	0.04	0.07	0.12	0.19	0.03	0.06	0.10	0.15	0.03	0.05	0.08	0.12	0.02	0.03	0.05	0.07	0.01	0.01	0.02	0.02
10.7	v		0.03	0.07	0.12	0.18	0.03	0.06	0.11	0.16	0.03	0.05	0.09	0.13	0.02	0.04	0.07	0.10	0.02	0.04	0.06	0.08	0.01	0.02	0.03	0.04	0.00	0.01	0.01	0.01
	h		0.05	0.10	0.19	0.28	0.05	0.09	0.18	0.26	0.04	0.08	0.15	0.20	0.04	0.07	0.12	0.16	0.03	0.06	0.10	0.13	0.02	0.04	0.06	0.07	0.01	0.01	0.02	0.03
18.7	v		0.04	0.08	0.14	0.19	0.04	0.07	0.12	0.17	0.03	0.06	0.10	0.13	0.03	0.05	0.08	0.10	0.02	0.04	0.06	0.08	0.01	0.02	0.03	0.04	0.00	0.01	0.01	0.01
	h		0.06	0.12	0.23	0.31	0.06	0.12	0.21	0.28	0.05	0.10	0.17	0.22	0.05	0.08	0.14	0.17	0.04	0.07	0.11	0.14	0.03	0.04	0.06	0.07	0.01	0.02	0.02	0.03
23.8	v		0.04	0.08	0.14	0.19	0.04	0.08	0.13	0.17	0.04	0.06	0.10	0.13	0.03	0.05	0.08	0.10	0.02	0.04	0.06	0.08	0.01	0.02	0.03	0.04	0.00	0.01	0.01	0.01
	h		0.07	0.14	0.24	0.32	0.06	0.13	0.22	0.28	0.06	0.11	0.18	0.22	0.05	0.09	0.14	0.18	0.04	0.07	0.11	0.14	0.03	0.05	0.07	0.08	0.01	0.02	0.02	0.03
37.0	v		0.05	0.09	0.15	0.19	0.04	0.08	0.13	0.17	0.04	0.07	0.11	0.13	0.03	0.06	0.08	0.10	0.03	0.04	0.06	0.08	0.01	0.02	0.03	0.03	0.00	0.00	0.00	0.00
	h		0.08	0.16	0.27	0.33	0.07	0.15	0.24	0.30	0.07	0.12	0.19	0.23	0.06	0.10	0.16	0.18	0.05	0.08	0.12	0.14	0.03	0.05	0.07	0.08	0.01	0.02	0.03	0.03
89.0	v		0.05	0.09	0.14	0.18	0.04	0.08	0.13	0.16	0.04	0.07	0.10	0.12	0.03	0.05	0.08	0.09	0.02	0.04	0.06	0.07	0.01	0.02	0.02	0.03	0.00	0.00	0.00	0.00
	h		0.10	0.21	0.31	0.36	0.10	0.19	0.28	0.32	0.09	0.16	0.23	0.25	0.07	0.13	0.18	0.20	0.06	0.11	0.14	0.15	0.04	0.06	0.08	0.08	0.02	0.02	0.03	0.03

TABLE XI
SAME AS TABLE VIII, BUT AT AN EIA OF 30°

f [GHz]	p	τ	0.95				0.90				0.80				0.70				0.60				0.40				0.20			
		W [m/s]	4	7	12	20	4	7	12	20	4	7	12	20	4	7	12	20	4	7	12	20	4	7	12	20	4	7	12	20
6.8	v		0.03	0.05	0.09	0.16	0.03	0.05	0.08	0.15	0.02	0.04	0.08	0.13	0.02	0.04	0.07	0.12	0.02	0.03	0.06	0.10	0.01	0.02	0.04	0.07	0.01	0.02	0.02	0.04
	h		0.03	0.06	0.10	0.19	0.03	0.05	0.10	0.18	0.03	0.05	0.09	0.16	0.02	0.04	0.08	0.14	0.02	0.04	0.07	0.12	0.02	0.03	0.05	0.08	0.01	0.02	0.03	0.05
10.7	v		0.03	0.06	0.10	0.19	0.03	0.05	0.10	0.18	0.03	0.05	0.09	0.16	0.03	0.05	0.08	0.14	0.02	0.04	0.07	0.12	0.02	0.03	0.05	0.08	0.01	0.02	0.03	0.04
	h		0.04	0.07	0.12	0.24	0.04	0.06	0.12	0.22	0.03	0.06	0.11	0.19	0.03	0.05	0.09	0.16	0.03	0.05	0.08	0.14	0.02	0.03	0.06	0.09	0.01	0.02	0.03	0.05
18.7	v		0.04	0.07	0.13	0.23	0.04	0.07	0.12	0.21	0.03	0.06	0.11	0.18	0.03	0.05	0.09	0.16	0.03	0.05	0.08	0.13	0.02	0.03	0.06	0.09	0.01	0.02	0.03	0.05
	h		0.04	0.08	0.15	0.29	0.04	0.08	0.15	0.26	0.04	0.07	0.13	0.22	0.04	0.06	0.11	0.19	0.03	0.06	0.10	0.16	0.02	0.04	0.07	0.10	0.01	0.02	0.04	0.06
23.8	v		0.04	0.07	0.14	0.25	0.04	0.07	0.13	0.23	0.04	0.06	0.11	0.19	0.03	0.06	0.10	0.16	0.03	0.05	0.09	0.14	0.02	0.04	0.06	0.09	0.01	0.02	0.03	0.05
	h		0.05	0.09	0.17	0.31	0.05	0.08	0.16	0.28	0.04	0.08	0.14	0.24	0.04	0.07	0.12	0.20	0.03	0.06	0.11	0.17	0.02	0.04	0.07	0.11	0.02	0.03	0.04	0.06
37.0	v		0.04	0.08	0.15	0.27	0.04	0.08	0.14	0.25	0.04	0.07	0.13	0.21	0.03	0.06	0.11	0.18	0.03	0.05	0.10	0.15	0.02	0.04	0.06	0.10	0.01	0.02	0.04	0.05
	h		0.05	0.10	0.19	0.34	0.05	0.10	0.18	0.31	0.05	0.09	0.16	0.26	0.04	0.08	0.14	0.22	0.04	0.07	0.12	0.18	0.03	0.05	0.08	0.12	0.02	0.03	0.05	0.07
89.0	v		0.05	0.09	0.18	0.30	0.05	0.09	0.17	0.28	0.04	0.08	0.15	0.23	0.04	0.07	0.13	0.20	0.04	0.06	0.11	0.16	0.03	0.04	0.07	0.10	0.02	0.03	0.04	0.06
	h		0.07	0.13	0.25	0.41	0.06	0.12	0.24	0.37	0.06	0.11	0.20	0.31	0.05	0.10	0.17	0.26	0.05	0.08	0.15	0.21	0.03	0.06	0.10	0.13	0.02	0.04	0.05	0.08

TABLE XII
SAME AS TABLE VIII, BUT AT AN EIA OF 0°

f [GHz]	τ	0.95				0.90				0.80				0.70				0.60				0.40				0.20			
	W [m/s]	4	7	12	20	4	7	12	20	4	7	12	20	4	7	12	20	4	7	12	20	4	7	12	20	4	7	12	20
6.8		0.02	0.04	0.08	0.14	0.02	0.04	0.08	0.13	0.02	0.04	0.07	0.12	0.02	0.04	0.07	0.11	0.02	0.03	0.06	0.10	0.02	0.03	0.05	0.08	0.01	0.02	0.03	0.05
10.7		0.03	0.05	0.09	0.16	0.03	0.05	0.09	0.16	0.03	0.05	0.08	0.15	0.02	0.04	0.08	0.13	0.02	0.04	0.07	0.12	0.02	0.03	0.05	0.09	0.01	0.02	0.04	0.06
18.7		0.03	0.06	0.11	0.20	0.03	0.06	0.11	0.19	0.03	0.06	0.10	0.18	0.03	0.05	0.09	0.16	0.03	0.05	0.08	0.14	0.02	0.04	0.06	0.11	0.02	0.03	0.05	0.07
23.8		0.04	0.07	0.12	0.22	0.04	0.06	0.12	0.21	0.03	0.06	0.11	0.19	0.03	0.06	0.10	0.17	0.03	0.05	0.09	0.15	0.02	0.04	0.07	0.11	0.02	0.03	0.05	0.08
37.0		0.04	0.07	0.14	0.25	0.04	0.07	0.13	0.24	0.04	0.07	0.12	0.22	0.04	0.06	0.11	0.20	0.03	0.06	0.10	0.17	0.03	0.04	0.08	0.12	0.02	0.03	0.05	0.09
89.0		0.05	0.09	0.17	0.31	0.05	0.09	0.16	0.30	0.05	0.08	0.15	0.27	0.04	0.08	0.13	0.24	0.04	0.07	0.12	0.21	0.03	0.05	0.09	0.15	0.02	0.04	0.06	0.10

that had been made in this paper compared with the values from [26]. The changes concern the expressions for the salinity dependence of the static dielectric constant $\varepsilon_S(T_S, S)$ and the first Debye relaxation frequency $f_1(T_S, S)$ in [26, eq. (17)]. Our new fit for $\varepsilon_S(T_S, S)$ is

$$\varepsilon_S(T_S, S) = \varepsilon_S(T_S, S=0) \cdot \exp[b_0 S + b_1 S^2 + B_2 T_S S]. \quad (29)$$

The updated values of the coefficients b_i, $i = 0$, 1, 2 are given in Table VI compared with the original values from [26, of Table VI]. The updated expression for the T_S, S-dependence of $f_1(T_S, S)$ is

$$f_1(T_S, S) = f_1(T_S, S=0) \cdot \left[1 + S \cdot (d_0 + d_1 T_S + d_2 T_S^2 + d_3 T_S^3 + d_4 t_s^4)\right] \quad (30)$$

with the coefficients d_i, $i = 0$, 1, 2, 3, 4 from Table VII. All other coefficients including the values for pure water $(S = 0)$ and the conductivity of sea water are the same as in [26].

APPENDIX B
VALUES FOR THE ATMOSPHERIC PATH LENGTH CORRECTION Ω

For reference, we want to give selected values of the atmospheric path length correction term Ω_p from Section V. For the computation, we have assumed that $T_S = T_{ref}$ and a typical atmospheric temperature of $T_D = 281$ K. Tables VIII–XII list the results for various values of the Earth incidence angle θ, frequency f, atmospheric transmittance τ, and wind speed W.

ACKNOWLEDGMENT

The authors would like to thank Peter Gaiser and Michael Bettenhausen (NRL, Washington, D.C.) for providing the WindSat Level 0 product.

REFERENCES

[1] C. L. Gentemann, T. Meissner, and F. J. Wentz, "Accuracy of satellite sea surface temperatures at 7 and 11 GHz," *IEEE Trans. Geosci. Remote Sens.*, vol. 48, no. 3, pp. 1009–1018, Mar. 2010.

[2] S. T. Wu and A. K. Fung, "A non-coherent model for microwave emission and backscattering from the sea surface," *J. Geophys. Res.*, vol. 77, no. 30, pp. 5917–5929, 1972.

[3] F. J. Wentz, "A two-scale scattering model for foam-free sea microwave brightness temperatures," *J. Geophys. Res.*, vol. 80, no. C24, pp. 3441–3446, Aug. 1975.

[4] S. H. Yueh, "Modeling of wind direction signals in polarimetric sea surface brightness temperatures," *IEEE Trans. Geosci. Remote Sens.*, vol. 35, no. 6, pp. 1400–1418, Nov. 1997.

[5] K. St. Germain, G. Poe, and P. Gaiser, "Modeling of polarimetric microwave signal due to ocean surface wind vector," in *Proc. IEEE Geosci. Remote Sens. Symp.*, Seattle, WA, 1998, vol. 5, pp. 2304–2306.

[6] J. Johnson, "An efficient two-scale model for the computation of thermal emission and atmospheric reflection from the sea surface," *IEEE Trans. Geosci. Remote Sens.*, vol. 44, no. 3, pp. 560–568, Mar. 2006.

[7] M. D. Powell, S. H. Houston, L. R. Amat, and N. Morisseau-Leroy, "The HRD real-time hurricane wind analysis system," *J. Wind Eng. Ind. Aerodyn.*, vol. 77/78, pp. 53–64, 1998.

[8] F. J. Wentz, "A well calibrated ocean algorithm for special sensor microwave/imager," *J. Geophys. Res.*, vol. 102, no. C4, pp. 8703–8718, 1997.

[9] F. J. Wentz, T. Meissner, AMSR ocean algorithm, version 2, Remote Sensing Systems, Santa Rosa, CA, 121 599A-1, 2000. [Online]. Available: http://www.remss.com/papers/amsr/AMSR_Ocean_Algorithm_Version_2.pdf

[10] T. Meissner and F. J. Wentz, "An updated analysis of the ocean surface wind direction signal in passive microwave brightness temperatures," *IEEE Trans. Geosci. Remote Sens.*, vol. 40, no. 6, pp. 1230–1240, Jun. 2002.

[11] T. Meissner and F. J. Wentz, "A radiative transfer model function for 85.5 GHz special sensor microwave imager ocean brightness temperatures," *Radio Sci.*, vol. 38, no. 4, pp. 8066–8073, Jun. 2003.
[12] T. Meissner and F. J. Wentz, "Ocean retrievals for WindSat: Radiative transfer model, algorithm, validation," in *Proc. 9th Spec. Meeting Microw. Radiometry Remote Sens. Appl.*, San Juan, PR, 2006, pp. 4761–4764, Paper Catalog # 06EX1174C.
[13] T. Meissner and F. J. Wentz, "Wind vector retrievals under rain with passive satellite microwave radiometers," *IEEE Trans. Geosci. Remote Sens.*, vol. 47, no. 9, pp. 3065–3083, Sep. 2009.
[14] T. Meissner, F. J. Wentz, and D. Draper, "GMI calibration algorithm and analysis theoretical basis document, version F," Remote Sensing Systems, Santa Rosa, CA, RSS Rep. 111 311, 2011.
[15] E. W. Uhlhorn, P. G. Black, J. L. Franklin, M. A. Goodberlet, J. R. Carswell, and A. S. Goldstein, "Hurricane surface wind measurements from an operational stepped frequency microwave radiometer," *Mon. Weather Rev.*, vol. 135, no. 9, pp. 3070–3085, Sep. 2007.
[16] S. F. El-Nimri, W. L. Jones, E. W. Uhlhorn, C. S. Ruf, J. Johnson, and P. G. Black, "An improved C-band ocean surface emissivity model at hurricane-force wind speeds over a wide range of earth incidence angles," *IEEE Geosci. Remote Sens. Lett.*, vol. 7, no. 4, pp. 641–645, Oct. 2010.
[17] P. Gaiser, K. M. St. Germain, E. M. Twarog, G. A. Poe, W. Purdy, D. Richardson, W. Grossman, W. L. Jones, D. Spencer, G. Golba, J. Cleveland, L. Choy, R. M. Bevilacqua, and P. S. Chang, "The WindSat spaceborne polarimetric microwave radiometer: Sensor description and early orbit performance," *IEEE Trans. Geosci. Remote Sens.*, vol. 42, no. 11, pp. 2347–2361, Nov. 2004.
[18] J. Hollinger, J. L. Peirce, and G. Poe, "SSM/I instrument description," *IEEE Trans. Geosci. Remote Sens.*, vol. 28, no. 5, pp. 781–790, Sep. 1990.
[19] A. Stogryn, "Estimates of brightness temperatures from scanning radiometer data," *IEEE Trans. Antennas Propag.*, vol. AP-26, no. 5, pp. 720–726, Sep. 1978.
[20] G. A. Poe, "Optimum interpolation of imaging microwave radiometer data," *IEEE Trans. Geosci. Remote Sens.*, vol. 28, no. 5, pp. 800–810, Sep. 1990.
[21] F. J. Wentz and T. Meissner, "AMSR-E ocean algorithms, version 2, supplement 1," Remote Sensing Systems, Santa Rosa, CA, Tech. Rep. 051 707, 2007.
[22] R. W. Reynolds and T. M. Smith, "Improved global sea surface temperature analyses using optimum interpolation," *J. Climate*, vol. 7, no. 6, pp. 929–948, Jun. 1994.
[23] C. Mears, D. K. Smith, and F. J. Wentz, "Comparison of special sensor microwave imager and buoy-measured wind speeds from 1987 to 1997," *J. Geophys. Res.*, vol. 106, no. C6, pp. 11 719–11 729, Jun. 2011.
[24] T. Meissner, D. K. Smith, and F. J. Wentz, "A 10-year intercomparison between collocated SSM/I oceanic surface wind speed retrievals and global analyses," *J. Geophys. Res.*, vol. 106, no. C6, pp. 11 731–11 742, Jun. 2001.
[25] F. J. Wentz and D. K. Smith, "A model function for the ocean-normalized radar cross section at 14 GHz derived from NSCAT observations," *J. Geophys. Res.*, vol. 104, no. C5, pp. 11 499–11 514, May 1999.
[26] T. Meissner and F. J. Wentz, "The complex dielectric constant of pure and sea water from microwave satellite observations," *IEEE Trans. Geosci. Remote Sens.*, vol. 42, no. 9, pp. 1836–1849, Sep. 2004.
[27] P. W. Rosenkranz, "Water vapor microwave continuum absorption: A comparison of measurements and models," *Radio Sci.*, vol. 33, no. 4, pp. 919–928, 1998.
[28] H. J. Liebe, P. W. Rosenkranz, and G. A. Hufford, "Atmospheric 60-GHz oxygen spectrum: New laboratory measurements and line parameters," *J. Quant. Spectrosc. Radiat. Transf.*, vol. 48, no. 5/6, pp. 629–643, Nov./Dec. 1992.
[29] M. J. Schwartz, *Observation and Modeling of Atmospheric Oxygen Millimeter-Wave Transmittance*. Cambridge, MA: MIT, 1997.
[30] V. H. Payne, E. J. Mlawer, K. E. Cady-Pereira, and J. L. Moncet, "Water vapor continuum absorption in the microwave," *IEEE Trans. Geosci. Remote Sens.*, vol. 49, no. 6, pp. 2194–2208, Jun. 2011.
[31] J. P. Hollinger, "Passive microwave measurements of sea surface roughness," *IEEE Trans. Geosci. Electron.*, vol. GE-9, no. 3, pp. 165–169, Jul. 1971.
[32] Y. Sasaki, I. Asanuma, K. Muneyama, G. Naito, and T. Suzuki, "The dependence of sea-surface microwave emission on wind speed, frequency, incidence angle, and polarization over the frequency range from 1 to 40 GHz," *IEEE Trans. Geosci. Remote Sens.*, vol. GE-25, no. 2, pp. 138–146, Mar. 1987.
[33] N. Tran, D. Vandemark, C. S. Ruf, and B. Chapron, "The dependence of nadir ocean surface emissivity on wind vector as measured with microwave radiometer," *IEEE Trans. Geosci. Remote Sens.*, vol. 40, no. 2, pp. 515–523, Feb. 2002.
[34] W. J. Webster, T. T. Wilheit, D. B. Ross, and P. Gloersen, "Spectral characteristics of the microwave emission from a wind-driven foam-covered sea," *J. Geophys. Res.*, vol. 81, no. 18, pp. 3095–3099, 1976.
[35] W. H. Peake, "Interaction of electromagnetic waves with some natural surfaces," *IEEE Trans. Antennas Propag.*, vol. AP-7, no. 5, pp. 324–329, Dec. 1959.
[36] C. S. Cox and W. H. Munk, "Measurement of the roughness of the sea surface from photographs of the sun's glitter," *J. Opt. Soc. Amer.*, vol. 44, no. 11, pp. 838–850, Nov. 1954.
[37] S. H. Yueh, R. Kwok, and S. V. Nghiem, "Polarimetric scattering and emission properties of targets with reflection symmetry," *Radio. Sci.*, vol. 29, no. 6, pp. 1409–1420, Nov./Dec. 1994.
[38] S. H. Yueh, W. J. Wilson, S. J. Dinardo, and F. K. Li, "Polarimetric microwave brightness signatures of ocean wind directions," *IEEE Trans. Geosci. Remote Sens.*, vol. 37, no. 2, pp. 949–959, Mar. 1999.
[39] S. H. Yueh, R. Kwok, F. K. Li, S. V. Nghiem, W. J. Wilson, and J. A. Kong, "Polarimetric passive remote sensing of ocean wind vectors," *Radio. Sci.*, vol. 29, no. 4, pp. 799–814, 1994.
[40] V. S. Etkin, M. D. Raev, M. G. Bulatov, Y. A. Militsky, and A. V. Smirnov, Radiohydrophysical aerospace research of ocean, Acad. Sci., Space Res. Inst., Moscow, Russia, Tech. Rep. IIp-1749, 1991.
[41] I. A. Renfrew, G. N. Petersen, D. A. J. Sproson, G. W. K. Moore, H. Adiwidjaja, S. Zhang, and R. North, "A comparison of aircraft-based surface-layer observations over Denmark Strait and the Irminger Sea with meteorological analyses and QuikSCAT winds," *Q. J. R. Meteorol. Soc.*, vol. 135, no. 645, pp. 2046–2066, Oct. 2009.

Thomas Meissner (M'02) received the B.S. degree in physics from the University of Erlangen-Nürnberg, Erlangen, Germany, in 1983, the M.S. (Diploma) degree in physics from the University of Bonn, Bonn, Germany, in 1987, and the Ph.D. degree in theoretical physics from the University of Bochum, Bochum, Germany, in 1991, writing his doctoral dissertation on effective quark models of the nucleon.

Between 1992 and 1998, he conducted postdoctoral research at the University of Washington, Seattle, the University of South Carolina, Columbia, and at Carnegie Mellon University, Pittsburgh, PA, in Theoretical Nuclear and Particle Physics focusing on the theory of strong interaction. In July 1998, he joined Remote Sensing Systems, Santa Rosa, CA. Since then, he has been working on the development and refinement of radiative transfer models, calibration, validation, and ocean retrieval algorithms for various microwave instruments (SSM/I, TMI, AMSR-E, WindSat, CMIS, SSMIS, GMI, Aquarius).

Dr. Meissner is on the review panel for the National Academies' Committee on Radio Frequencies.

Frank J. Wentz received the B.S. and M.S. degrees in physics from the Massachusetts Institute of Technology, Cambridge, in 1969 and 1971, respectively.

In 1974, he established Remote Sensing Systems, a research company specializing in satellite microwave remote sensing of the Earth. His past research focused on radiative transfer models that relate satellite observations to geophysical parameters, with the objective of providing reliable geophysical data sets to the Earth science community. As a member of the NASA's SeaSat Experiment Team (1978–1982), he pioneered the development of physically based retrieval methods for microwave scatterometers and radiometers. Starting in 1987, he took the lead on providing the worldwide research community with high-quality ocean products derived from satellite microwave imagers. As the President of RSS, he oversees the production and validation of climate-quality satellite products. These data are dispersed via the company's web and FTP sites. He is currently a member of the NASA Advanced Microwave Scanning Radiometer Team, NASA Ocean Vector Wind Science Team, and NASA REASoN DISCOVER Project. He has served on many NASA review panels, and the National Research Council's Earth Studies Board, and the National Research Council's Panel on Reconciling Temperature Observations. He is a lead author for CCSP Synthesis and Assessment Product on Temperature Trends in the Lower Atmosphere. He is currently working on scatterometer/radiometer combinations, satellite-derived decadal time series of atmospheric moisture and temperature, the measurement of sea-surface temperature through clouds, and advanced microwave sensor designs for climatological studies.

Dr. Wentz is a member of the American Geophysical Union.